

Supplementary Information

Optically Accessible Long-Lived Electronic Biexcitons at Room Temperature in Strongly Coupled H-aggregates

Siddhartha Sohoni^{1, 2, 3, 4, 5}, Indranil Ghosh^{1, 2, 3, 4, 5}, Geoffrey T. Nash¹, Claire A. Jones^{1, 2, 3, 4}, Lawson T. Lloyd^{1, 2, 3, 4}, Beiye C. Li^{1, 2, 3, 4}, Karen L. Ji^{1, 2, 3}, Zitong Wang¹, Wenbin Lin¹, Gregory S. Engel^{1, 2, 3, 4 *}

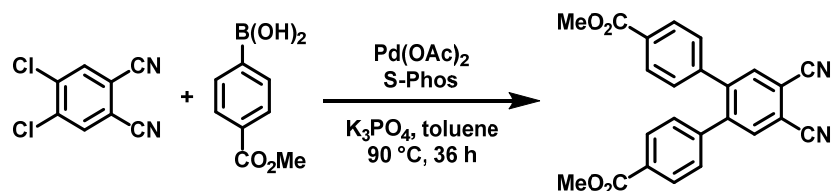
1. Department of Chemistry, The University of Chicago, Chicago, IL 60637, USA
2. The Institute for Biophysical Dynamics, The University of Chicago, Chicago, IL 60637, USA
3. James Franck Institute, The University of Chicago, Chicago, IL 60637, USA
4. Pritzker School for Molecular Engineering, The University of Chicago, Chicago, IL 60637, USA
5. contributed equally

Corresponding author: gsengel@uchicago.edu

Suppl. Note 1. Materials synthesis and characterization

All chemical reagents were purchased from commercial sources and used without further purification as follows: 4,5-dichlorophthalonitrile (Tokyo Chemical Industry), 4-(methoxycarbonylphenyl)-boronic acid (Boron Molecular), palladium(II) acetate (Pd(OAc)₂; Thermo Scientific Chemicals), 2-Dicyclohexylphosphino-2',6'-dimethoxybiphenyl (S-Phos; Sigma-Aldrich), 1,8-diazabicyclo[5.4.0]undec-7-ene (DBU; Oakwood Chemical). Transmission electron microscopy (TEM) was performed on a TECNAI TEM (120 kV), and high-resolution TEM (HR-TEM) was performed on a TECNAI F30 TEM (300 kV). Atomic force microscopy (AFM) was performed on a Bruker Multimode 8-HR AFM. Powder X-ray diffraction (PXRD) patterns were obtained on a Bruker D8 Venture diffractometer using a Cu K α radiation source (λ = 1.54178 Å) and processed with PowderX software. Dynamic light scattering (DLS) measurements were obtained on a Malvern Zetasizer Nano ZS instrument. ¹H and ¹³C NMR spectra were collected on a Bruker NMR 400 DRX spectrometer at 400 MHz and 101 MHz, respectively, and referenced to the proton resonance resulting from incomplete deuteration of CDCl₃ (δ 7.26). Matrix-assisted laser desorption/ionization-time of flight high resolution mass spectrometry (MALDI-TOF HRMS) was performed on a Bruker autoflex maX MALDI-TOF/TOF using negative-ion reflectron mode.

1.1. Synthesis and characterization of ZnOPPC acid



Synthesis of 4,5-Bis(4-methoxycarbonylphenyl)phthalonitrile

4,5-bis(4-methoxycarbonylphenyl)phthalonitrile was synthesized as previously reported with minor modifications.¹ An oven-dried Schlenk tube was charged with 4,5-dichlorophthalonitrile (2.00 g, 10.2 mmol), 4-(methoxycarbonylphenyl)-boronic acid (5.4 g, 30.0 mmol), Pd(OAc)₂ (44 mg, 0.2 mmol), S-Phos (200 mg, 0.5 mmol), anhydrous K₃PO₄ (8.48 g, 40.0 mmol), and a stir bar. The reaction vessel was sealed and backfilled with nitrogen three times. Anhydrous toluene (40 mL) was added, and the mixture was stirred at 90 °C for 36 h. After cooling to room temperature, toluene (~80 mL) was added, and the reaction mixture was filtered and washed twice with water. The combined organic layers were dried over anhydrous Na₂SO₄ and then concentrated under vacuum. The crude product was purified by column chromatography using CHCl₃/hexanes/EtOAc (4:4:1) and recrystallized from EtOAc to afford the pure product as white crystals (2.11 g, 52% yield).

^1H NMR (400 MHz, CDCl_3): δ 7.97 (d, J = 8.6 Hz, 4H), 7.91 (s, 2H), 7.19 (d, J = 8.6 Hz 4H), 3.94 (s, 6H)

^{13}C NMR (101 MHz, CDCl_3): δ 166.21, 144.85, 141.58, 135.38, 130.46, 129.99, 129.41, 115.28, 114.99, 52.39.

TLC: R_f = 0.44 (CHCl_3 /hexanes/EtOAc 4:4:1)

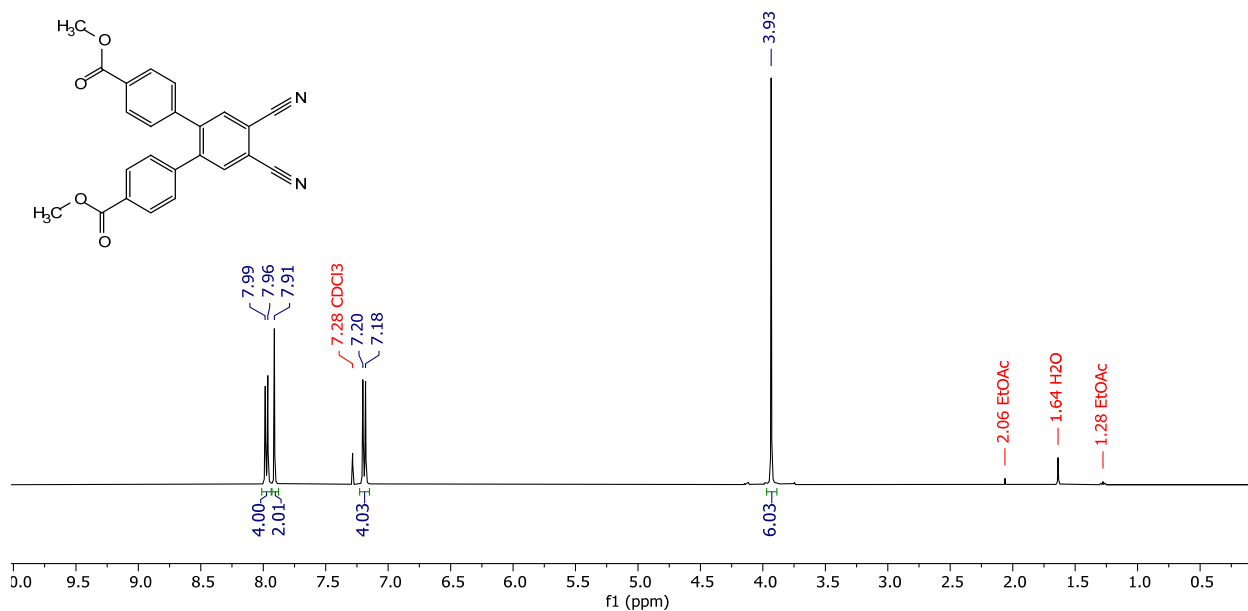


Figure S1. ^1H NMR of 4,5-bis(4-methoxycarbonylphenyl)phthalonitrile (400 MHz, CDCl_3).

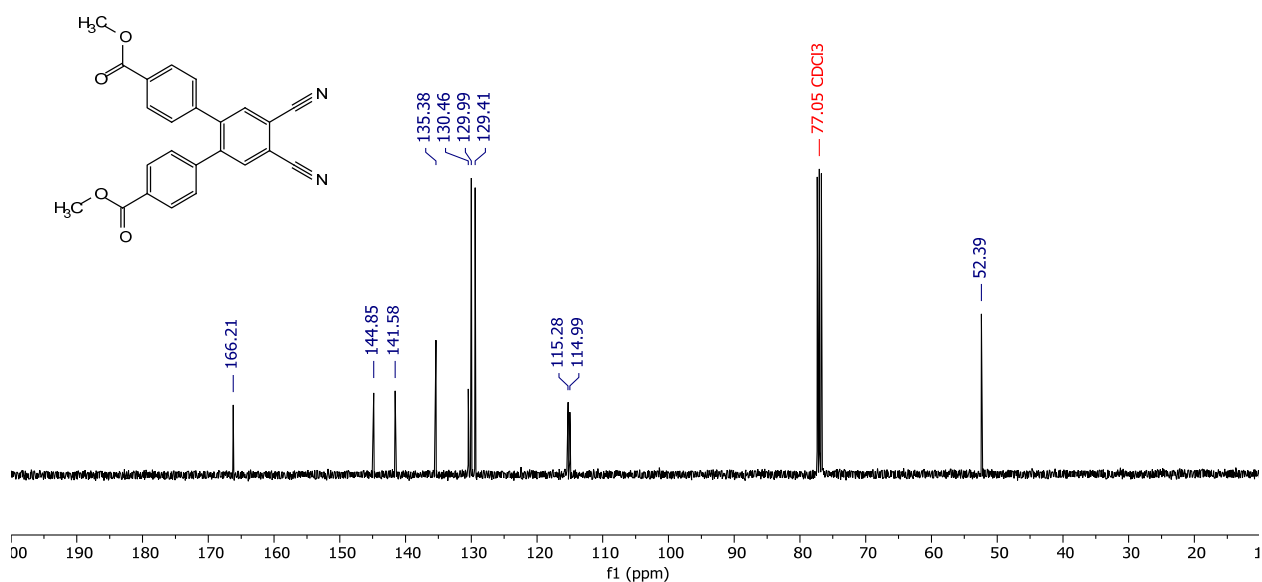
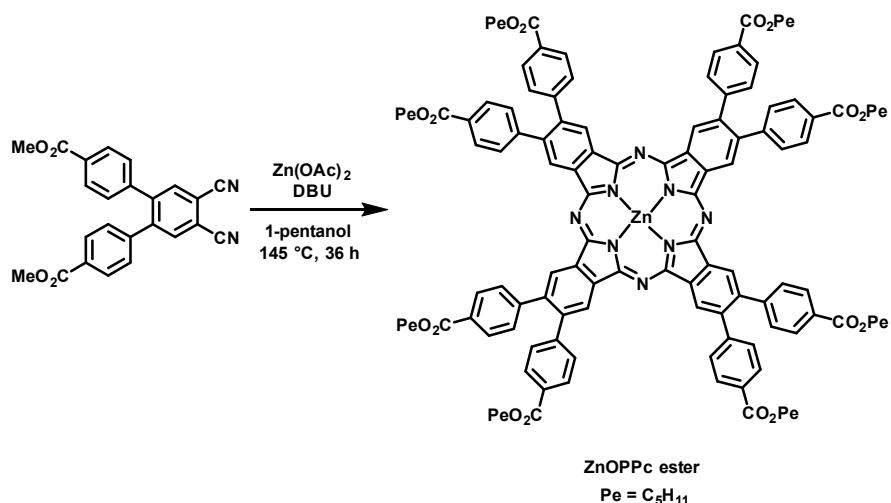


Figure S2. ^{13}C NMR of 4,5-bis(4-methoxycarbonylphenyl)phthalonitrile (101 MHz, CDCl_3).



Synthesis of zinc(II) 2,3,9,10,16,17,23,24-octa[4-pentoxycarbonylphenyl] phthalocyanine (ZnOPPc ester)

ZnOPPc ester was synthesized as previously reported with minor modifications.¹ A mixture of 4,5-bis(4-methoxycarbonylphenyl)phthalonitrile (800 mg, 2.02 mmol), anhydrous Zn(OAc)₂ (93 mg, 0.507 mmol), DBU (301 μ L, 2.02 mmol) and anhydrous 1-pentanol (30 mL) was added to a 100 mL round-bottomed flask and refluxed under nitrogen for 36 h. The reaction mixture was cooled to room temperature and MeOH (60 mL) was added to the reaction mixture and stirred for a further 30 min. The precipitated solid was collected by centrifugation, washed twice with MeOH/H₂O (4:1), once with MeOH, and thrice with acetonitrile. The crude product was purified by column chromatography using CHCl₃/EtOAc (4:1). The first dark green fraction was collected and dried under vacuum to yield a dark green solid (823 mg, 19% yield).

HRMS (MALDI-TOF): m/z Calcd. for C₁₂₈H₁₂₈N₈O₁₆Zn⁺ (M⁺): 2096.87, Found: 2096.765.

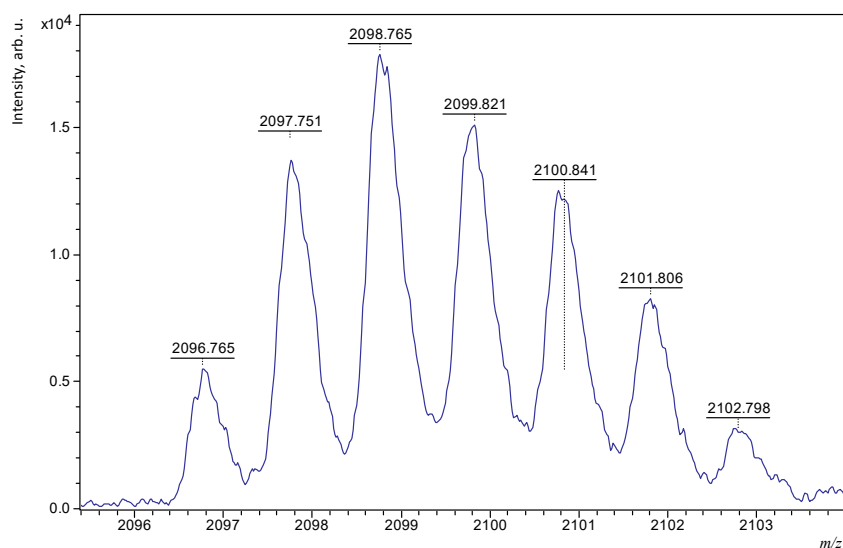
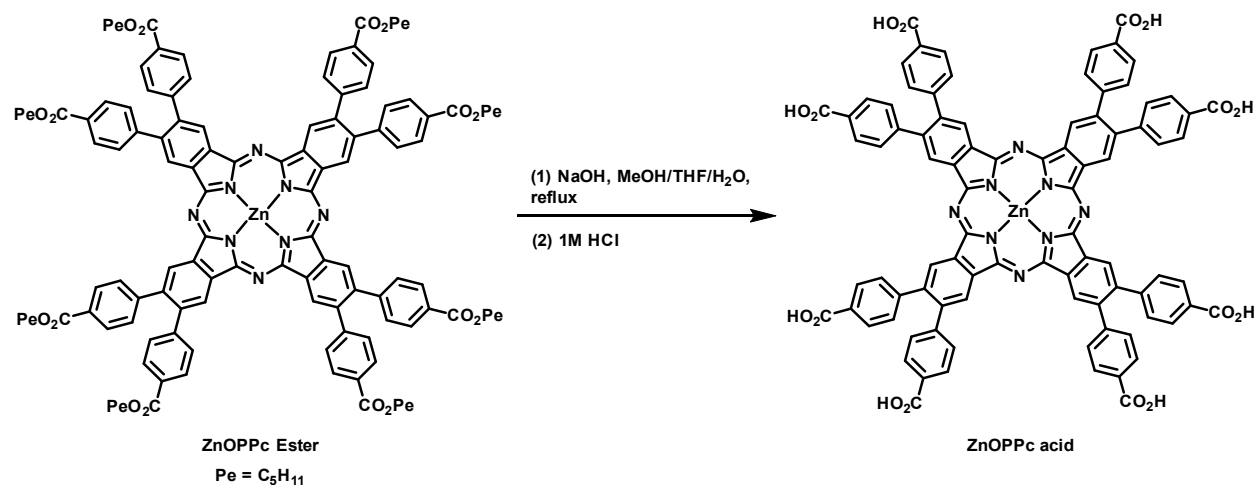


Figure S3. HRMS (MALDI-TOF) spectrum of ZnOPPc ester showing the isotopic peaks of the molecular ion [M⁺].



Synthesis of zinc(II) 2,3,9,10,16,17,23,24-octa[4-carboxyphenyl] phthalocyanine (ZnOPPc acid)

ZnOPPc acid was synthesized as previously reported with minor modifications.¹ A mixture of ZnOPPc ester (300 mg) and THF/MeOH (100 mL, 1:1) was added to an aq. NaOH solution (2.90 g/40 mL H₂O) and ultrasonicated. The mixture was then refluxed for 24 h. The reaction mixture was cooled to room temperature and the volatile solvents were removed under vacuum. H₂O (80 mL) was added to the solution and acidified, using 1 M HCl, until pH = 3. The precipitated solid was collected by centrifugation and washed with H₂O/MeOH (2:1), acetone, EtOAc, and DCM. The product was then dried under vacuum overnight to yield a dark green solid (200 mg, 91% yield).

HRMS (MALDI-TOF): m/z Calcd. for $\text{C}_{88}\text{H}_{48}\text{N}_8\text{O}_{16}\text{Zn}^+$ (M^+): 1536.25, Found: 1536.202.

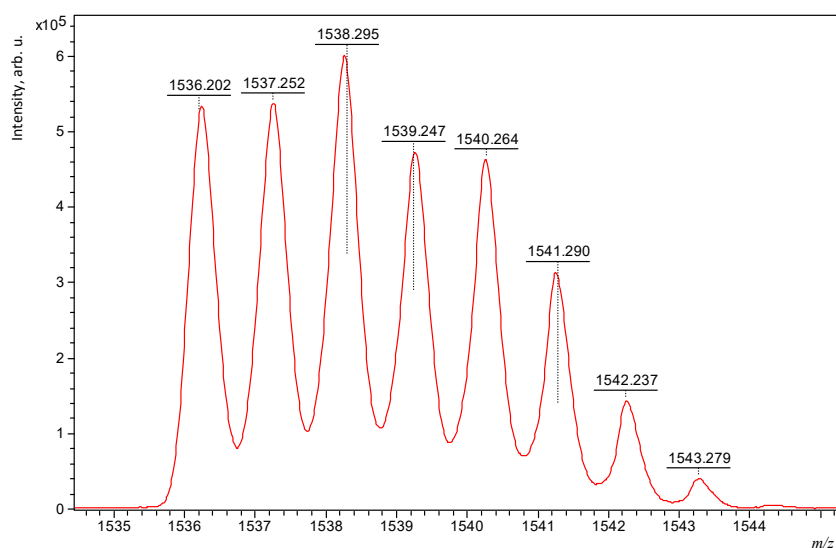


Figure S4. HRMS (MALDI-TOF) spectrum of ZnOPPc acid showing the isotopic peaks of the molecular ion [M^+].

1.2. Synthesis and characterization of neutral ZnOPPc aggregate

Self-assembly of neutral ZnOPPc aggregate via vapor diffusion

ZnOPPc acid (5 mg, 3.25 μmol) was added to a 2 mL vial and fully dissolved in a minimum amount of DMSO using sonication. The vial was capped with foil and then the foil was punctured with several small holes. The vial was carefully placed into a larger 20 mL vial and ~ 4 mL water was added to the bottom of the 20 mL vial. The larger vial was sealed and placed into an oven set at 80 $^{\circ}\text{C}$ for 24 hours. The large vial was removed, cooled to room temperature, and then the neutral ZnOPPc aggregate particles were collected from the smaller vial.

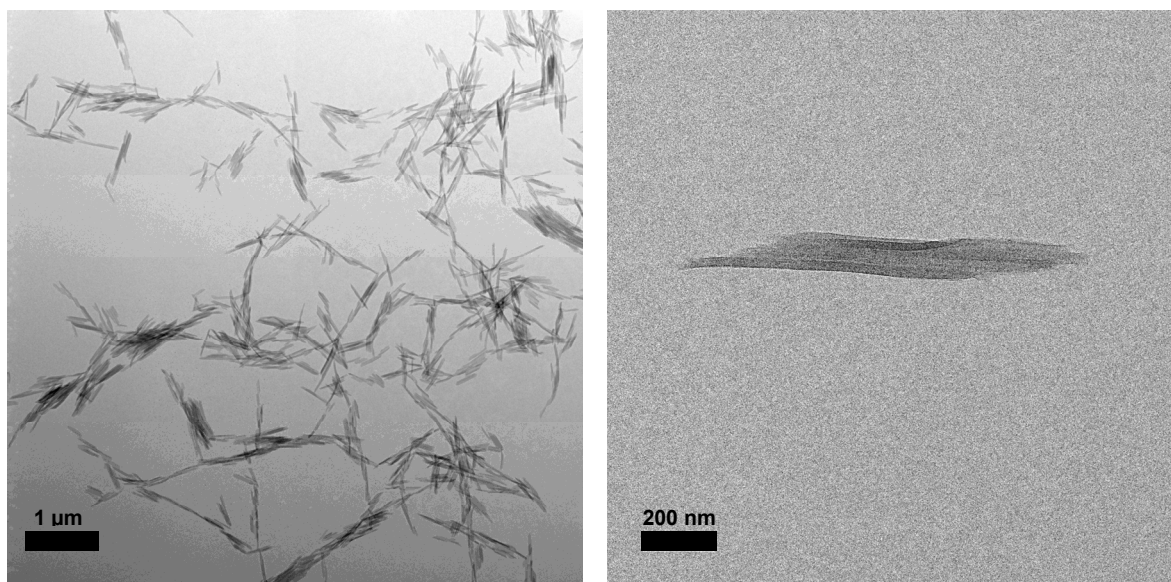


Figure S5. TEM images of the framework of connected aggregates.

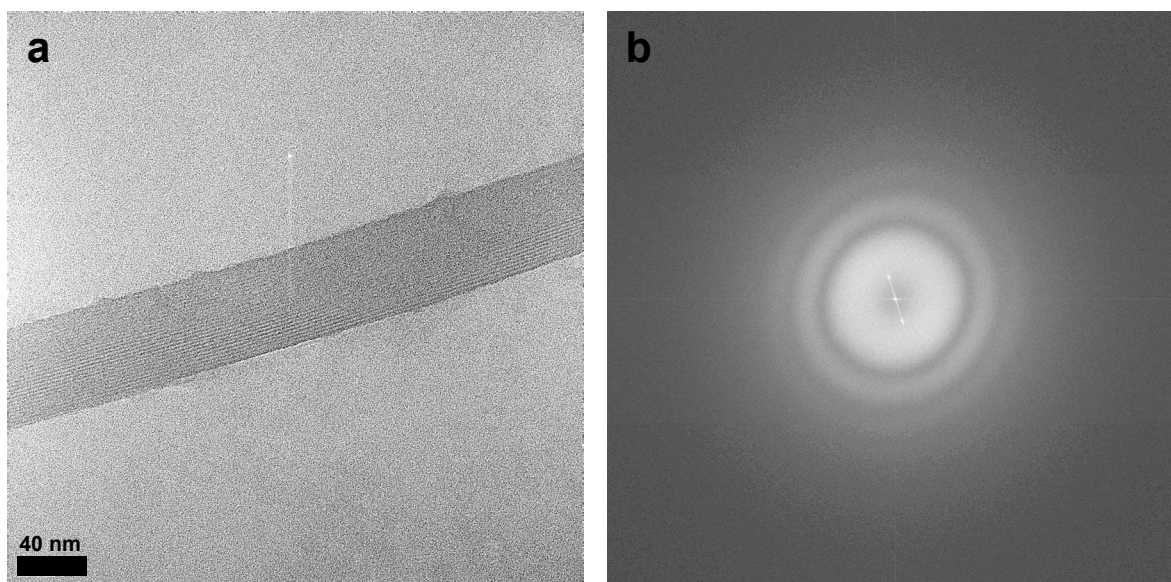


Figure S6. (a) HR-TEM image of the framework with its (b) FFT showing two-fold symmetry; this is consistent with a projection of π - π stacking along the length of the rod and hydrogen bonding between lattice fringes across the width of the rod.

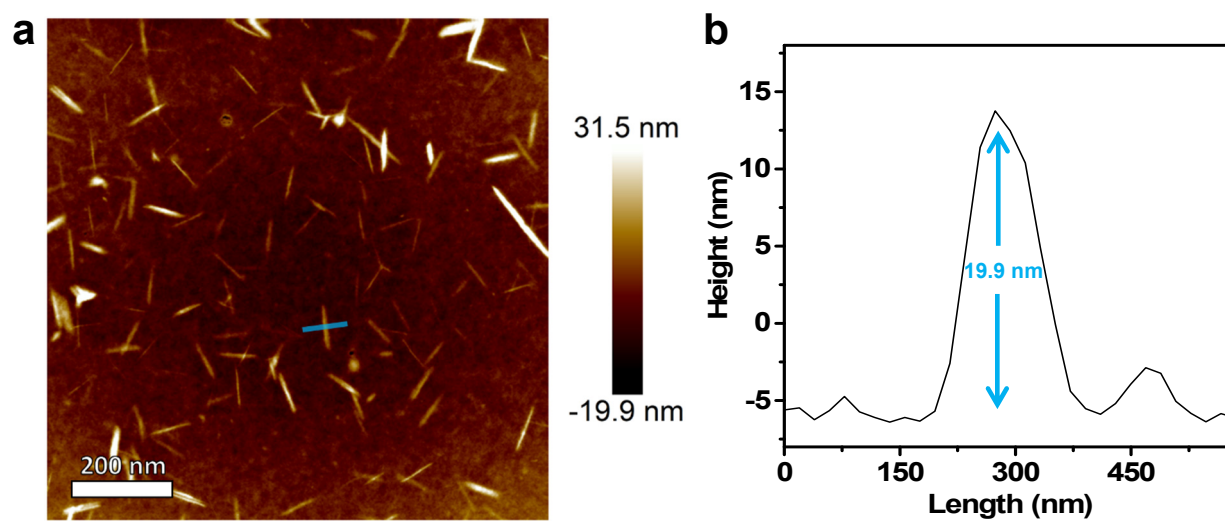


Figure S7. (a) AFM topographic image of the framework of aggregates and (b) measured height profile of a selected particle.

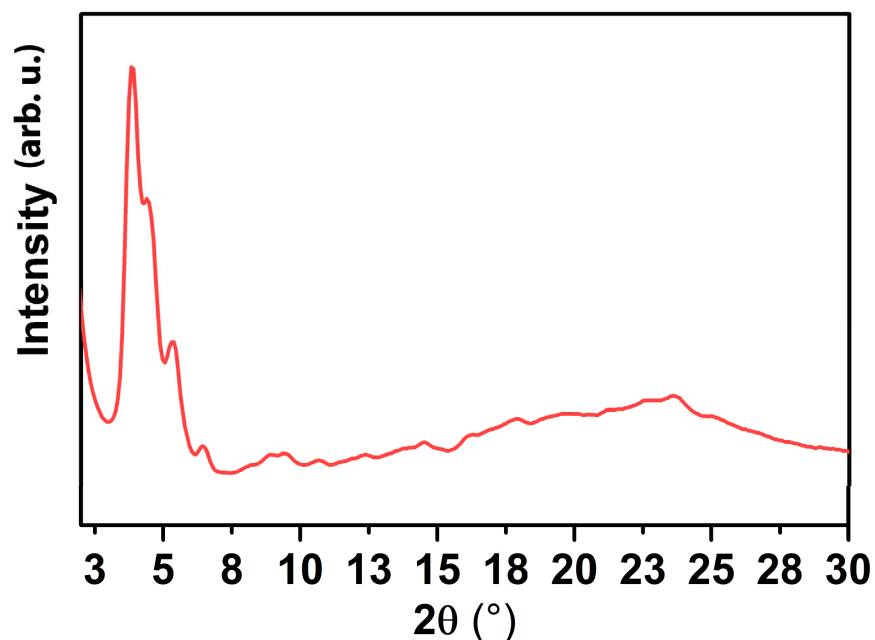


Figure S8. PXRD pattern of the framework of aggregates: X-ray powder diffraction patterns were collected in transmission mode using the SAXSLab Ganesha instrument (XENOCs) equipped with a Xenocs GeniX3D Cu K α X-ray source (1.5418 Å). Samples were loaded into 0.8-1.1 mm ID, 0.25 mm wall borosilicate capillaries and sealed with wax under nitrogen. Data reduction and integration were performed using the Saxsgui software.

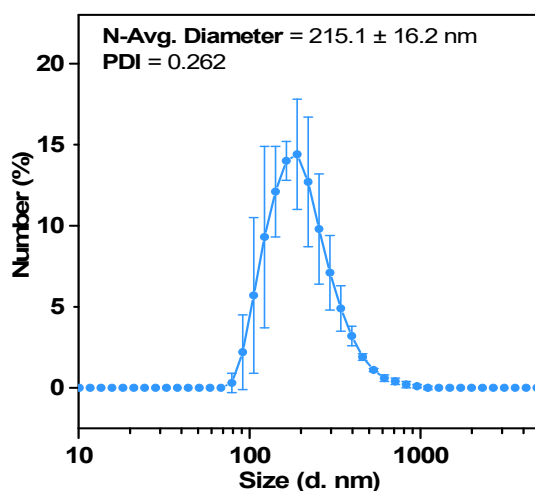


Figure S9. Number-averaged diameter and polydispersity index (PDI) for a water dispersion of the ZnOPPC aggregate framework, measured by DLS. Error bars represent 95% confidence intervals across 3 measurement runs. Each measurement is split into a series of 30 sub-runs, of which only 50% with the lowest mean count rates are used in the analysis.

1.3. Characterization of basic ZnOPPC aggregate

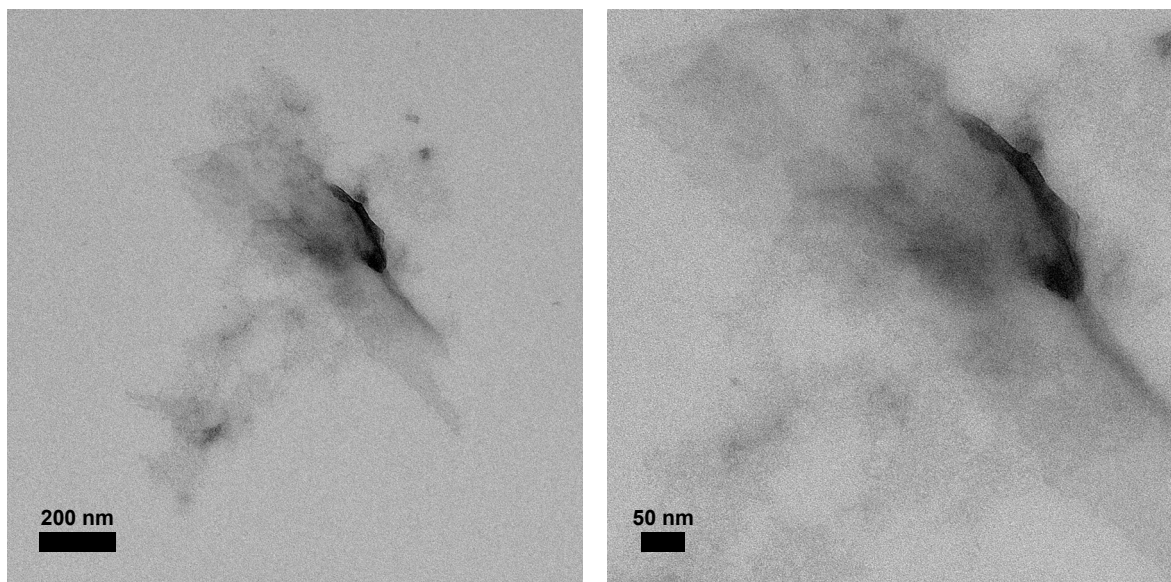


Figure S10. TEM images of a solution of single aggregates, showing the most aggregated regions of the grid.

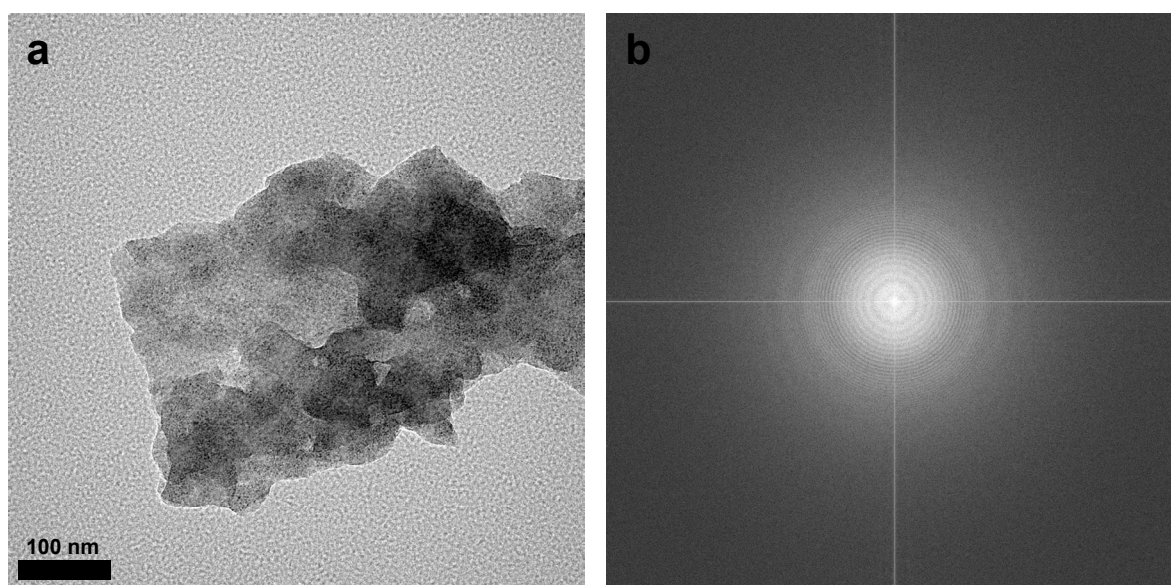


Figure S11. (a) HR-TEM image of single aggregates with its (b) FFT pattern, confirming that the basic aggregates lack long-range order.

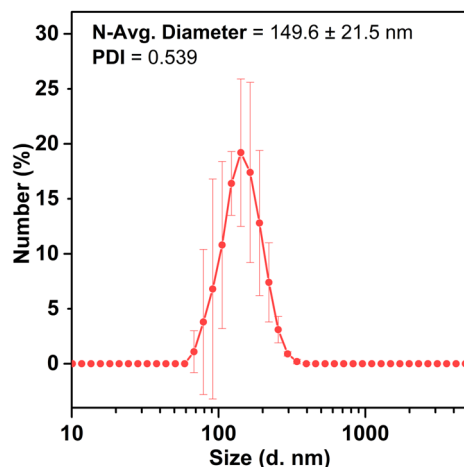


Figure S12. Number-averaged diameter and polydispersity index (PDI) for a water dispersion of the ZnOPPc basic aggregate, measured by DLS. Error bars represent 95% confidence interval across 3 measurement runs. Each measurement is split into a series of 30 sub-runs, of which only 50% with the lowest mean count rates are used in the analysis.

1.4. Acid-Base titration of the ZnOPPc aggregates

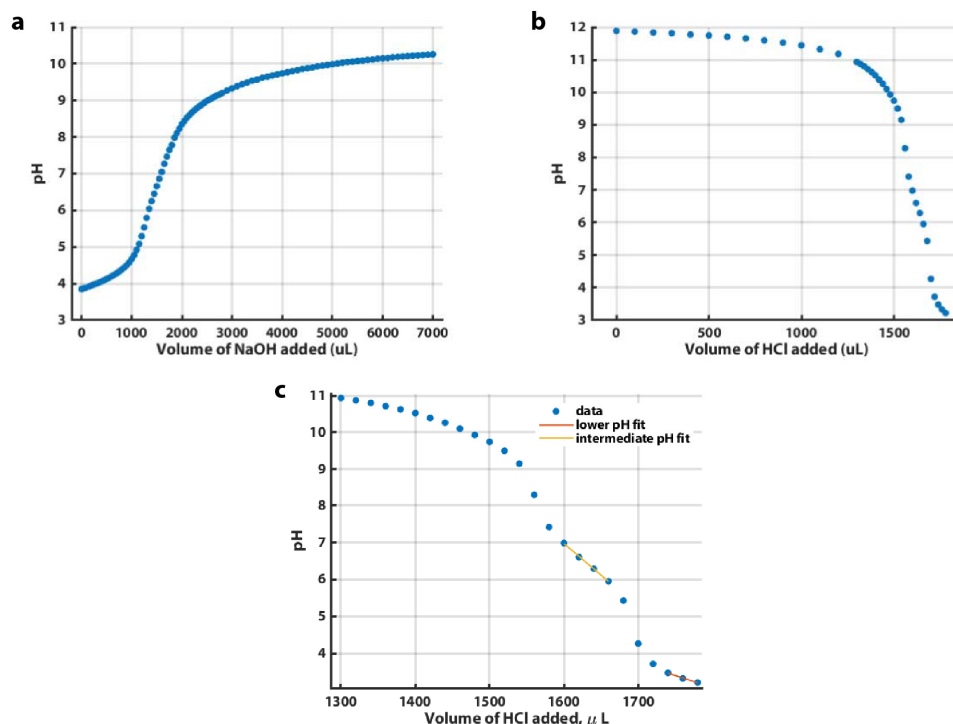


Figure S13. (a) Titration of acidic ZnOPPc aggregates at an initial pH of 3.85 with aqueous NaOH (pH = 10.92). (b) Titration of basic ZnOPPc aggregates at an initial pH of 11.88 with aqueous HCl (pH = 1.26). (c) Inflection regions of the data shown in part **b** shown with linear fits to the buffer regions with R^2 values of > 0.99 .

Acid-base titrations were performed on the ZnOPPc aggregate to better understand the pH dependent chemical changes to our system. ZnOPPc acid powder (3.43 mg) was first dissolved in a minimal amount of DMSO and sonicated at room temperature in a water bath for 90 minutes. A concentrated neutral ZnOPPc aggregate solution was then prepared by adding 5 drops of the ZnOPPc acid monomer solution and 10 drops of deionized water in a large vial followed by sonication for 5 minutes. The neutral ZnOPPc aggregate solution was subsequently diluted through addition of 15 mL of deionized water. Immediately prior to the titrations, aqueous HCl or aqueous NaOH was added to two neutral ZnOPPc aggregate solutions to modify the pH to be 3.85 and 11.88, respectively. A pH electrode (Oakton pH 5 Acorn series) was then submerged in the acidic or basic ZnOPPc aggregate solution and the pH was recorded after small amounts of aqueous HCl or NaOH stock solutions were added under stirring.

The titration curve of acidic ZnOPPc aggregates with aqueous NaOH is sigmoidal in shape with an equivalence point at pH 7 (Figure S13a). This resembles what is expected for the titration of free HCl in solution with aqueous NaOH. Thus, there is no obvious deprotonation of the carboxylic acid groups of the acidic ZnOPPc aggregates upon addition of NaOH. This is in stark contrast with the titration curve of the basic ZnOPPc aggregates with aqueous HCl, which shows two clear equivalence points at pHs of approximately 5 and 8 as well as two linear buffer regions from pH 3.22-3.48 and 5.95-6.98 (Figure S13b). The difference in shape between the titration curves of acidic and basic ZnOPPc aggregates suggests that we are titrating two different chemical species. Figure S13a likely corresponds to the titration of acidic ZnOPPc aggregate framework which eventually breaks up in high pH conditions at the end of the titration. The titration of basic ZnOPPc aggregates should initially start with disordered aggregates in solution; however, it is possible that these disordered aggregates are in a kinetic trap in which the H-bonded framework expected for neutral ZnOPPc aggregates is not restored upon decreasing the pH during the titration. If this is the case, the titration of the disordered basic ZnOPPc aggregates which do not have hydrogens involved in the formation of a hydrogen-bonded framework should better reflect the acid-base chemistry of the free ZnOPPc acid monomer. Performing a linear regression analysis of the buffer regions (pH 3.22-3.48 and 5.95-6.98) of the basic ZnOPPc titration curve and calculating the expected pH at the midpoints of these buffer regions, we estimate pKa values of 3.34 and 6.46 (Figure S13c). These pKa values are in the expected range for hydrogens of carboxylic acid groups and therefore likely correspond to protonation of the hydrogens on the carboxylic acid groups of the ZnOPPc acid monomers of the disordered aggregates.

1.5. Aggregate linear absorption spectra as a function of pH

Additional titrations were performed in conjunction with linear absorption measurements to spectroscopically characterize the effect of changing pH on the ground-state electronic structure of the ZnOPPc aggregates. A pH electrode (Oakton pH 5 Acorn series) was submerged in an aqueous neutral ZnOPPc aggregate solution, and the pH of the solution was adjusted to approximately 4 through the addition of aqueous HCl (pH 1.4). During the titration, small amounts of aqueous NaOH (pH 12.9) were added to the solution under stirring while the pH of the solution was measured. At selected pH values, an aliquot of the ZnOPPc aggregate solution was pipetted into a 1 mm quartz cuvette and its UV-Vis absorption spectrum was taken on a Cary 5000 UV-Vis-NIR spectrometer. After the absorption spectrum was taken, the ZnOPPc solution in the cuvette was transferred back to the original solution and titration with NaOH was resumed. There was some drift of the pH electrode from the time the UV-Vis spectrum was taken and the time the titration was resumed; however, this pH drift was relatively small, with the maximum magnitude being

0.15. For consistency, we have reported the pH values read at the time that the UV-Vis absorption spectrum was taken for all spectra.

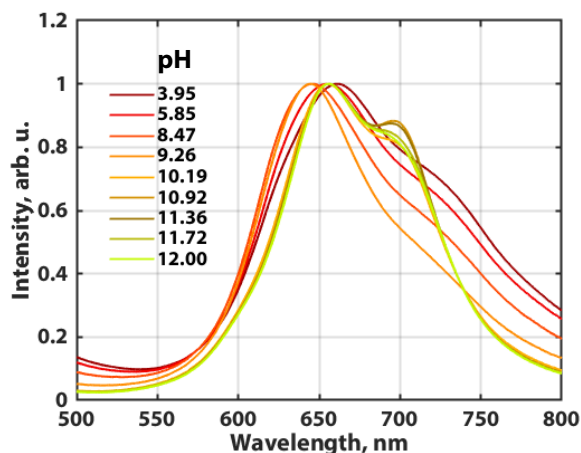


Figure S14. Normalized linear absorption spectra of the aggregate solution as a function of pH.

Figure S14 shows normalized linear absorption spectra of aqueous ZnOPPc aggregates taken at different pH points during titration with NaOH. All spectra consist of the main aggregate absorption peak at approximately 650 nm as well as a vibronic shoulder located at 700 nm. From pH 3.95 to 9.26, an increase in pH results in a blueshift of the aggregate absorption maximum from 662 nm to 647 nm. The magnitude of the blueshift of the aggregate absorption maximum from the monomer absorption maximum (700 nm) can be interpreted as the magnitude of coupling between monomers through face-to-face π -stacking in the ZnOPPc aggregates from pH 3.95 to 9.26. Although we cannot definitively assign a cause to this increase in coupling, we speculate that at the most acidic pH, protonation of nitrogen atoms on the phthalocyanine ring of ZnOPPc may lead to positive charge buildup on the monomers. This increased charge would result in electrostatic repulsion which would increase the distance between monomers and decrease coupling. As the pH is raised from 3.95 to 9.26, decreased protonation would lead to the increased H-aggregation evident in our absorption spectra. From pH 9.26 to 10.19, there is an abrupt redshift in the absorption maximum from 647 nm to 655 nm. We speculate that in this pH range, the carboxylic acids that hold together the HOF finally deprotonate leading the aggregates to separate and the increased charge on the monomers in these isolated aggregates decreases coupling leading to the observed redshift. From pH 10.26 to 12.00, there are only slight changes in the UV-Vis absorption spectra of the ZnOPPc aggregates, suggesting that changes to electronic structure with increasing pH are negligible in this regime.

The consistent appearance of a shoulder peak around 700 nm (the expected position of the monomer Q-band transition) in the linear absorption spectrum of both neutral and basic ZnOPPc aggregate solutions leads us to question whether aggregates and monomers coexist in appreciable amounts in aqueous solution. We conducted linear absorption measurements on neutral and basic aggregate solutions of different concentrations that were prepared through serial dilution. The reasoning behind the experiment is noted below.

We observe narrowing of the spectral features when changing from pH 9.26 to 10.19. We attribute this narrowing to decreased static disorder. We cannot definitively assign the origin of this disorder, but it likely arises from one of two sources in the HOF samples: either disorder amongst the aggregate environments within the extended HOF or disorder within individual aggregates due to the partial

protonation of the monomer carboxylic acid groups. Destruction of the extended HOF and the resulting full deprotonation of the carboxylic acid groups reduces the static disorder leading to narrowing of the aggregate peaks in the linear absorption spectrum.

We calculate that each H-aggregate in the extended HOF contains 11 ± 3 ZnOPPC monomers. This value for the electronic delocalization represents a lower bound for the physical size of the aggregate. Therefore, we can write an approximate equilibrium expression for the process of disaggregation as follows:

$$\text{ZnOPPC}_{\text{aggregate}} \rightarrow 11 \text{ ZnOPPC}_{\text{monomer}}$$

$$K_{\text{eq}} = \frac{[\text{ZnOPPC}_{\text{monomer}}]^{11}}{[\text{ZnOPPC}_{\text{aggregate}}]}$$

Equation S1.1

Suppose a solution of ZnOPPC aggregates and monomers at equilibrium was diluted by a factor of n . We can calculate the reaction quotient, Q , for this process as follows:

$$Q = \frac{\left(\frac{[\text{ZnOPPC}_{\text{monomer}}]}{n}\right)^{11}}{\left(\frac{[\text{ZnOPPC}_{\text{aggregate}}]}{n}\right)} = K_{\text{eq}} \left(\frac{1}{n}\right)^{10}$$

Equation S1.2

Upon dilution, Q would become less than K_{eq} . To restore equilibrium, we would expect that more monomer would be formed. This evolution of free monomer would manifest in our absorption spectra as the growth of a relatively sharp peak at 700 nm compared to the main aggregate peak at approximately 650 nm. We do observe such a peak as we transition from an acidic/neutral aggregate (HOF) to a basic aggregate (isolated aggregate) as is evident in Figure 1 of the main text and in Figure S14. However, titrations performed below in Figure S15 suggest that no free monomer population exists in our solution, meaning that that feature is likely vibronic structure amplified by H-aggregation.

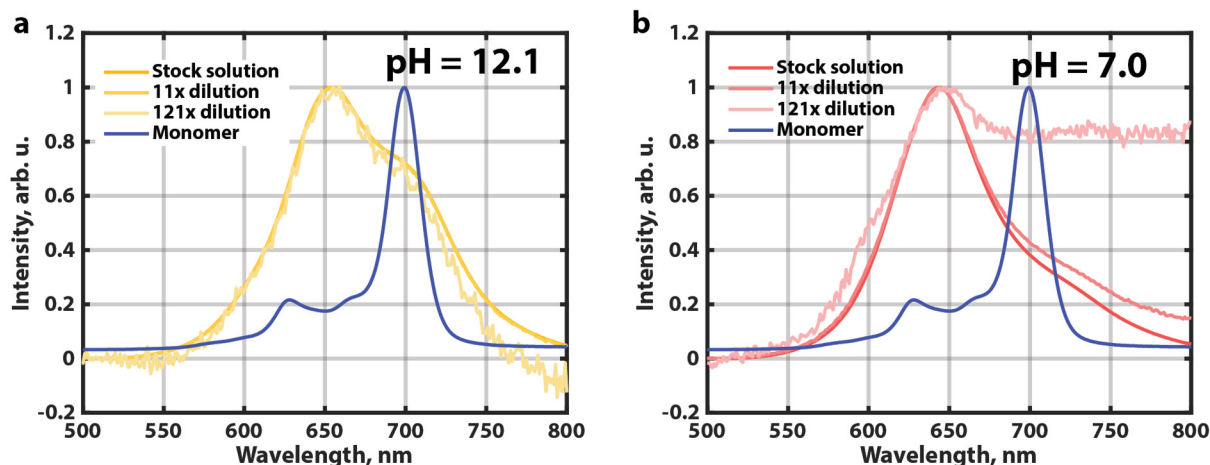


Figure S15. Normalized aggregate linear absorption spectral variation with concentration at (a) pH 12.1 and (b) pH 7.0. The normalized monomer spectrum is shown in both figures for context.

Figure S15 shows normalized linear absorption spectra of a series of aqueous neutral and basic aggregate solutions prepared to be different concentrations through serial dilutions by a factor of 11. The neutral aggregate solutions were prepared and diluted with phosphate-buffered saline (HyQ[®] DPBS), while basic aggregate solutions were prepared and diluted with an NaOH stock solution of pH 12.1. The pH values of all neutral and basic aggregate solutions were in the ranges of 6.97-7.00 and 12.09-12.14, respectively, which eliminates potential effects of changing pH on the ground state electronic structure. Peaks at 650 nm

and the red shoulder at ~ 700 nm are visible in the absorption spectra of both basic and neutral aggregates even after dilution by a factor of 121, although the spectra of aggregate solutions diluted by a factor of 121 display visible noise. Upon diluting the neutral aggregate solution, there is a slight increase in relative intensity of the 700 nm peak; however, the shape of the spectrum does not significantly change. Thus, we attribute this increase in relative intensity of the 700 nm to a drift of the baseline during the experiment which is evident from the increased absorbance in the 700-800 nm region of the spectrum in more dilute solutions. Upon dilution of the basic aggregates, we see no increase in relative intensity of the 700 nm peak compared to the 650 nm peak. In fact, the spectra of the basic aggregate stock solution and the basic aggregate solution diluted by a factor of 11 are nearly identical. Therefore, we conclude that the peak at 700 nm in the aggregate spectrum is a vibronic shoulder and not due to monomer absorption. Furthermore, we conclude that aggregates and monomers do not coexist in appreciable amounts in aqueous solution.

Suppl. Note 2. Spectroscopic methods and pulse characterization

Ultrafast transient absorption (TA) and two-dimensional electronic spectroscopy (2DES) experiments were conducted using sub-10 fs ultrabroadband pulses (Figure S16). Detailed description of the nonlinear spectrometer has been reported previously.² Briefly, a mode-locked oscillator (Coherent, Inc.) with a Ti:Sapphire crystal that operates at 80 MHz seeds a Ti:Sapphire regenerative amplifier (Coherent, Inc.), which in turn generates a ~ 40 fs pulse centered at 800 nm with a 5 kHz repetition rate. This pulse undergoes self-phase modulation in a pressurized 2 m long argon gas tube to create chirped white broadband pulses with a bandwidth ranging from 480 nm to 780 nm. Dichroic filters, bandpass filters (Thorlabs, Inc.) and chirp mirrors (Laser Quantum) are used to shape the bandwidth and temporal profile of the pulse. This results in a sub-10 fs pulse with a bandwidth from 500 nm to 780 nm.

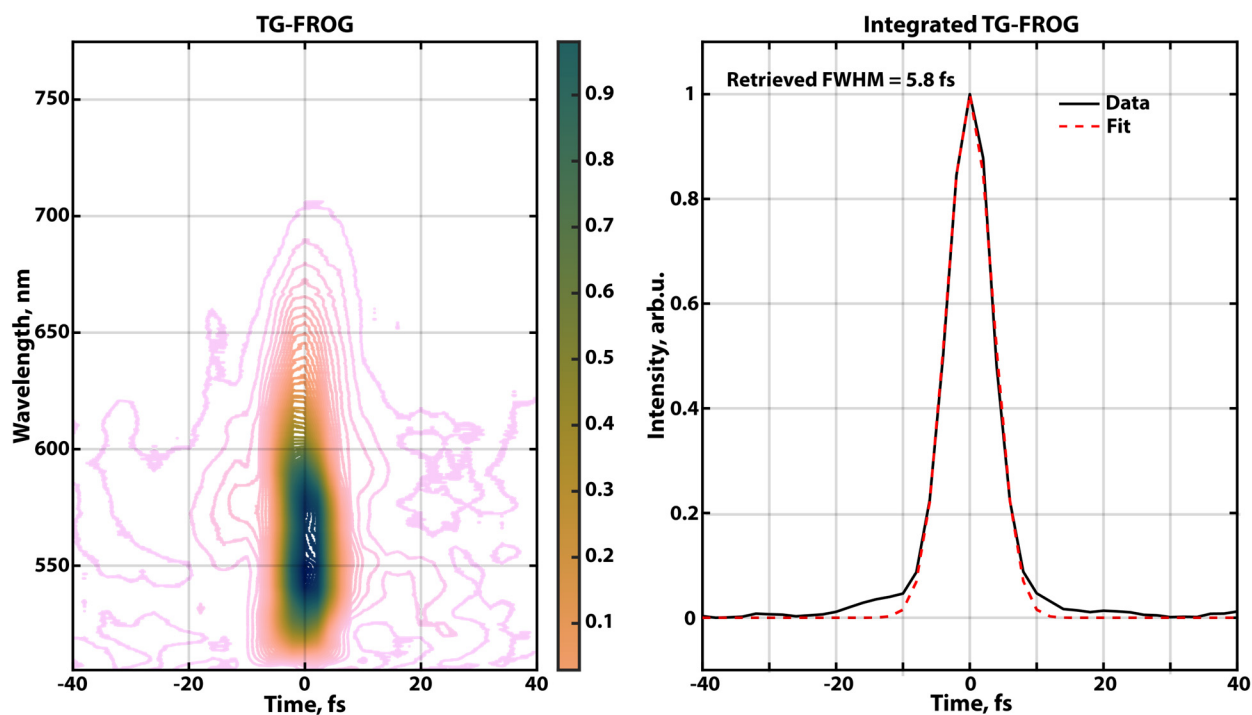


Figure S16. Femtosecond pulse characterization. TG-FROG measurement at the sample position in a glass slide in the ‘BOXCARS’ 2DES experimental geometry. The spectrogram was integrated over wavelength and fit with a Gaussian function which estimated a full-width half-maximum (FWHM) of ~ 8.2 fs, corresponding to a pulse FWHM of ~ 5.8 fs.

Suppl. Note 3. Additional two-dimensional electronic spectroscopy data

3.1. Additional 2DES spectra

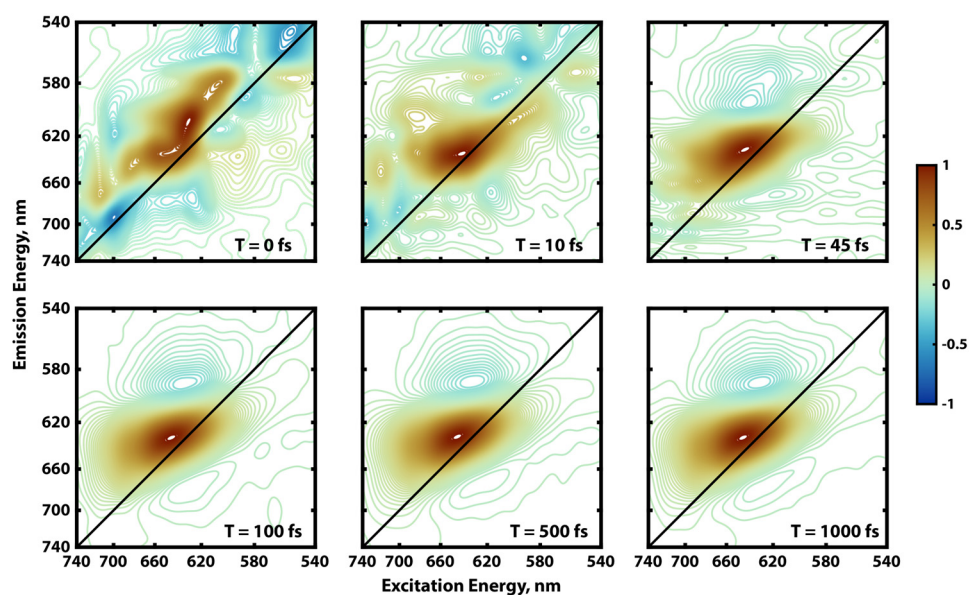


Figure S17. Additional 2DES frames with all-parallel pulse sequence of the framework of aggregates. Each frame is normalized to itself.

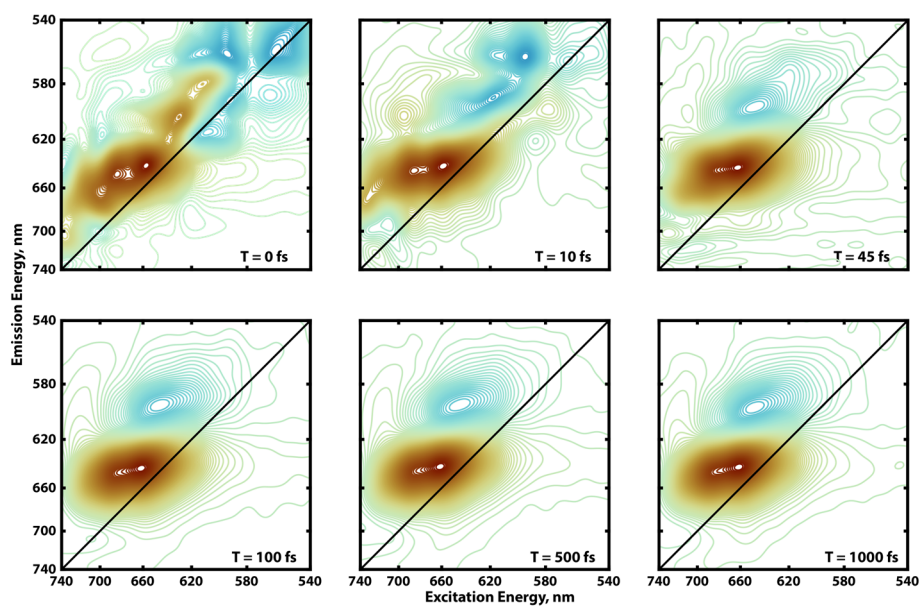


Figure S18. Additional 2DES frames with all-parallel pulse sequence of isolated aggregates. Each frame is normalized to itself.

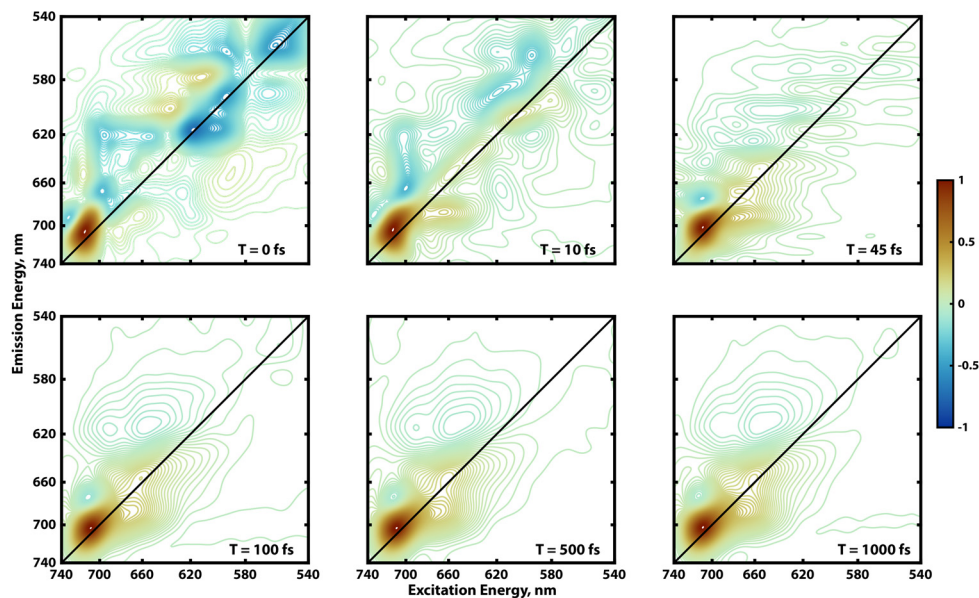


Figure S19. 2DES frames of the ZnOPPC monomer in DMSO with all-parallel pulse sequence. Each frame is normalized to itself.

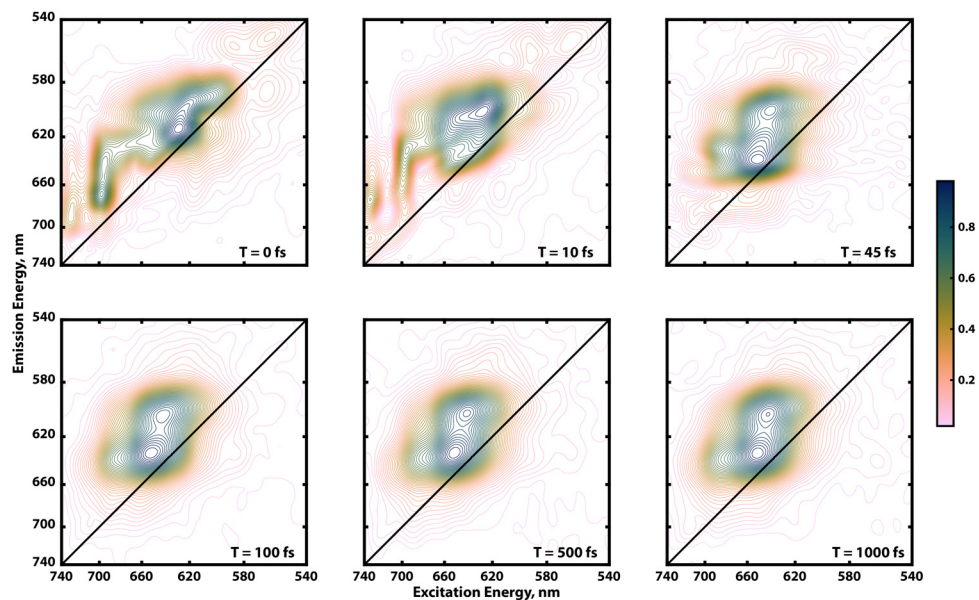


Figure S20. Additional absolute value 2DES frames with the $(90,60,120,0)^\circ$ pulse sequence for the framework of aggregates. Each frame is normalized to itself.

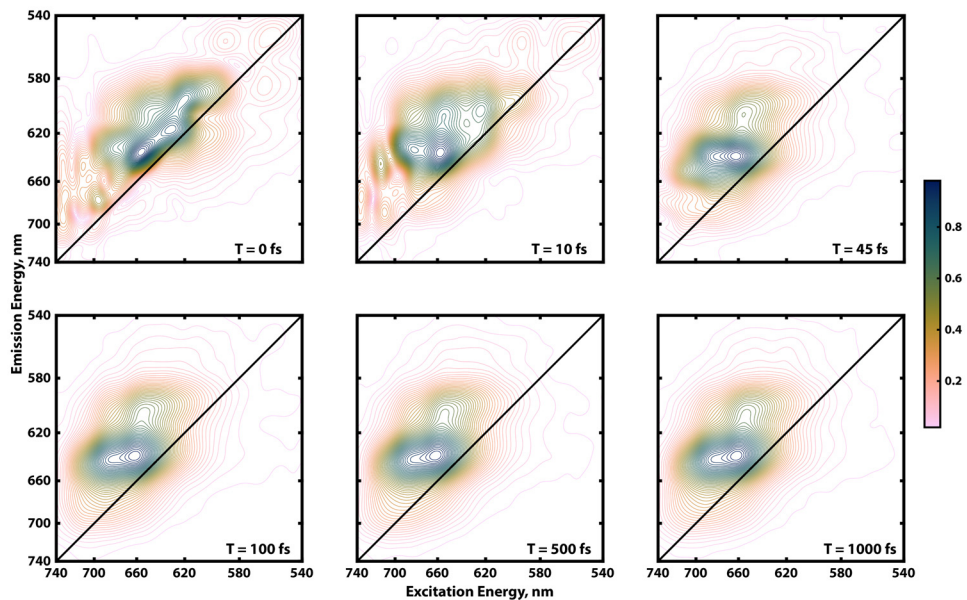


Figure S21. Additional absolute value 2DES frames with the $\langle 90,60,120,0 \rangle^\circ$ pulse sequence for isolated aggregates. Each frame is normalized to itself.

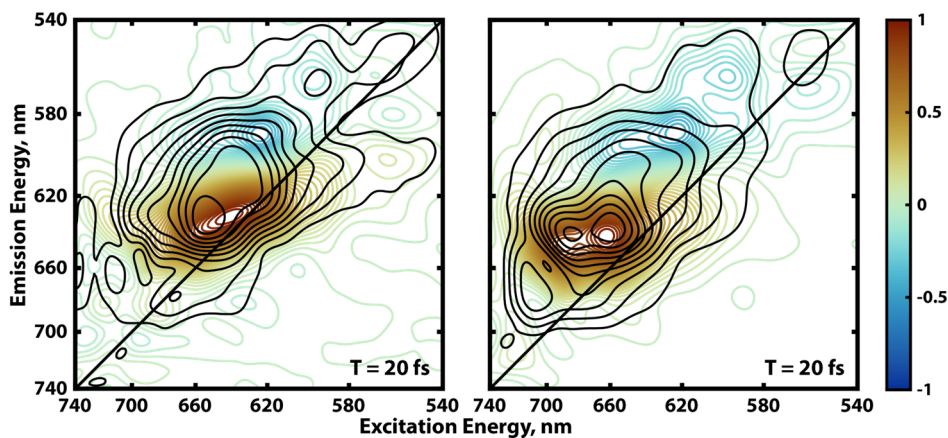


Figure S22. Overlay of the real-valued phased 2DES spectrum with parallelly polarized pulses (colored contours) with its absolute-valued 2DES spectrum of the cross-peak specific pulse sequence (black contours) for the framework of aggregates (left) and isolated aggregates (right). This how the derivative lineshape in the all-parallel spectrum masks and distorts the biexciton feature.

3.2 Linewidth analysis of 2DES spectra

Center Line Slope (CLS) analysis is a proxy for the frequency-frequency correlation function and its evolution in waiting time primarily indicates spectral diffusion. The slope can also inform about static and dynamic disorder in the frequency distribution of the excitonic system.³

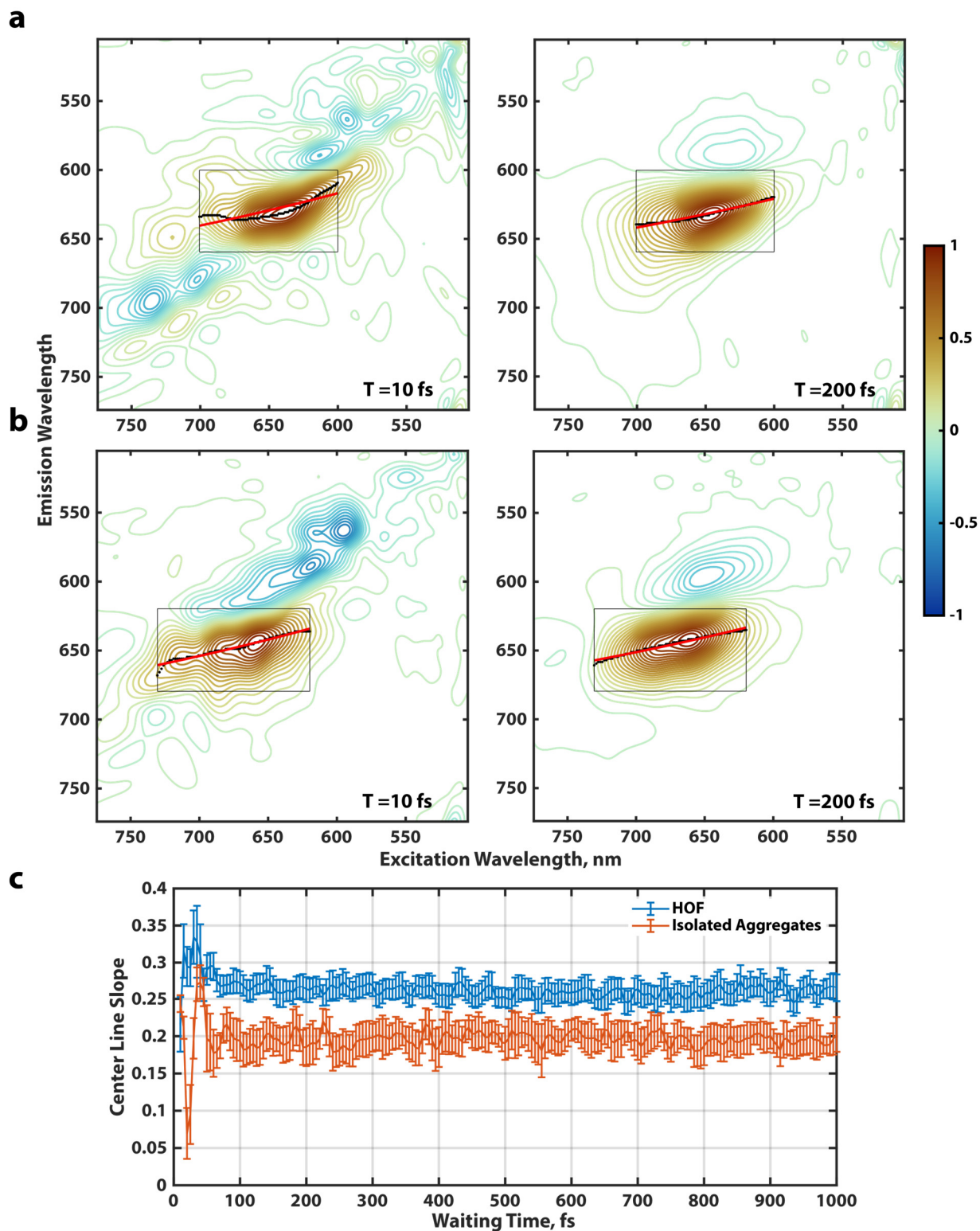


Figure S23. CLS fits to the ground state bleach feature for the (a) framework of aggregates and (b) isolated aggregates for one experimental run. (c) CLS as a function of waiting time in the sub-ps timescale for both aggregate systems. HOF averaged over 10 datasets and isolated aggregates averaged over 5 datasets. Error bars are 1 standard error in the mean.

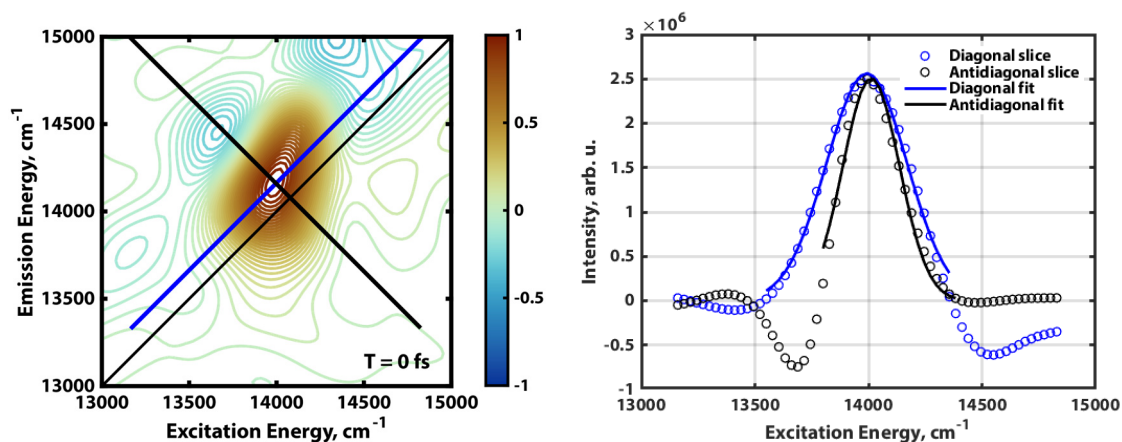


Figure S24. Gaussian fits of the diagonal and antidiagonal slices of the ground state bleach feature of the monomer 2DES spectrum at waiting time zero. The FWHM values from the diagonal and antidiagonal fits are 295 cm^{-1} and 207 cm^{-1} respectively – indicating an inhomogeneous broadening of 88 cm^{-1} .

Suppl. Note 4. Transient absorption data and kinetic analysis

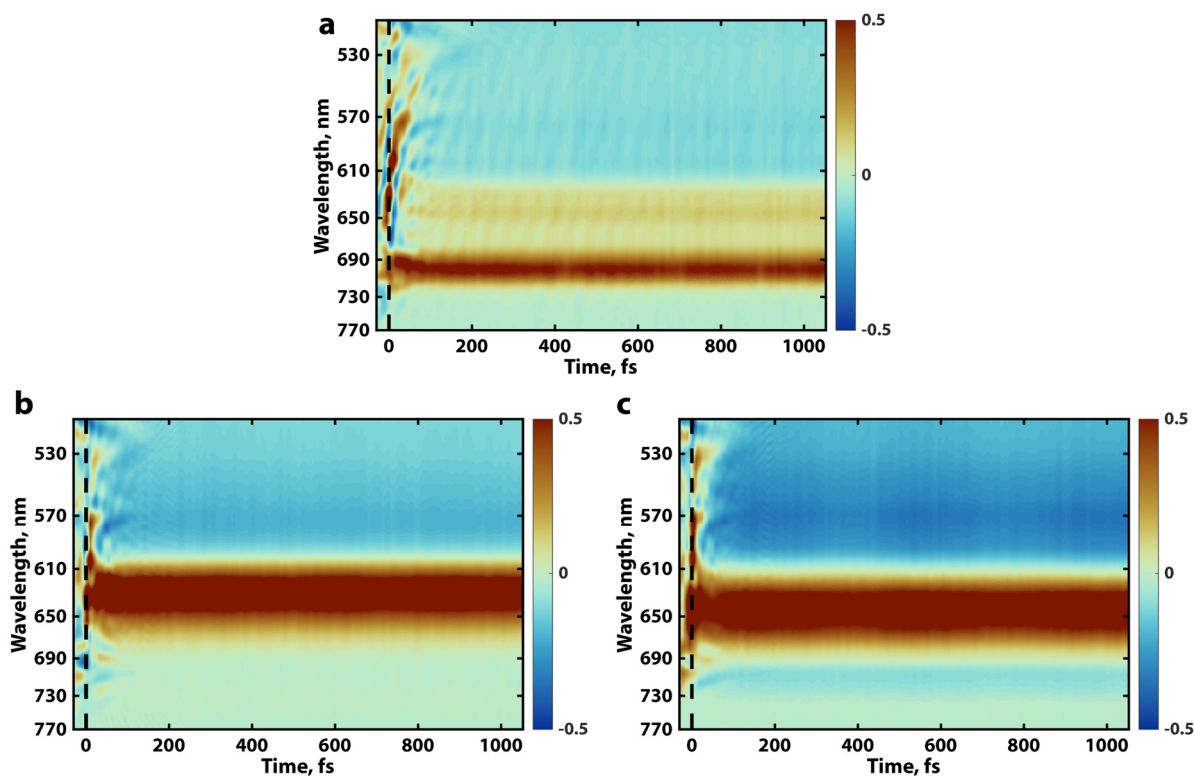


Figure S25. Transient absorption spectrum with a pump fluence of 20 nJ up to 1 ps for (a) monomer, (b) HOF and (c) isolated aggregates. These were used to phase the corresponding 2DES spectra.

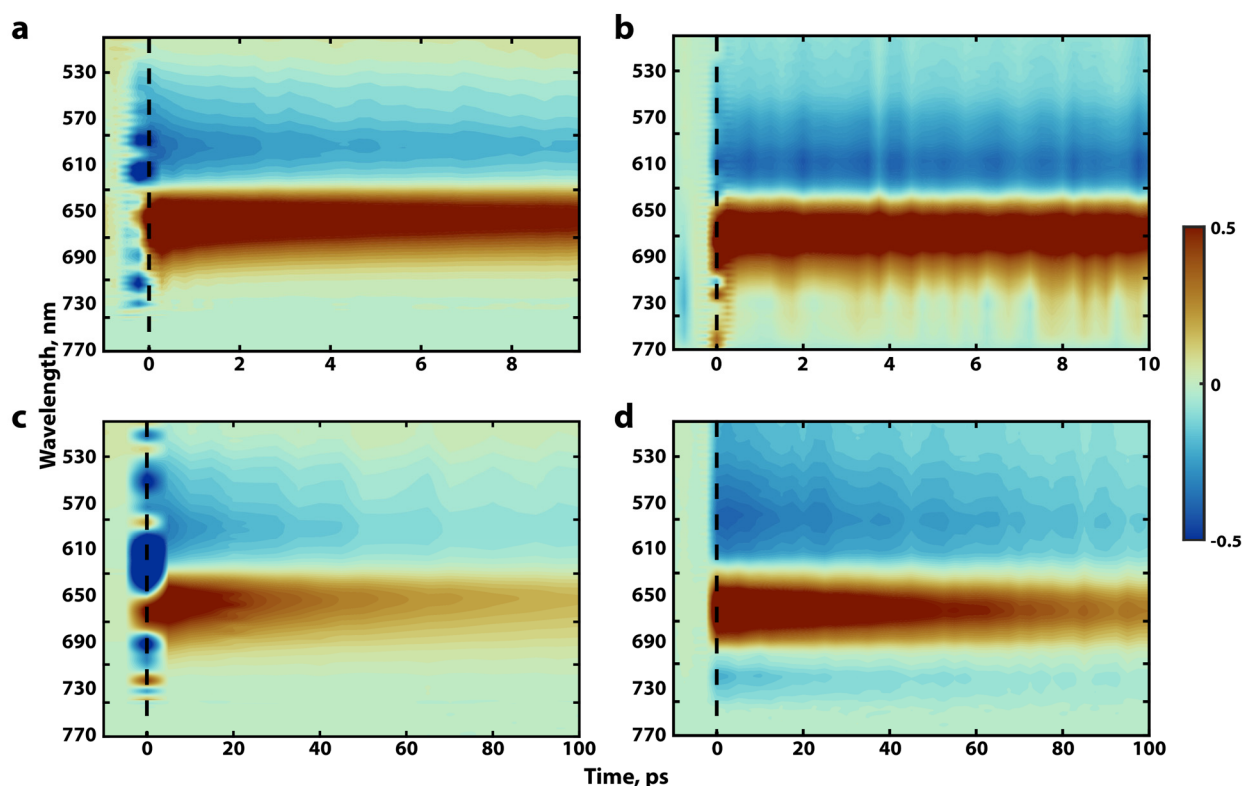


Figure S26. Transient absorption spectrum of the framework of aggregates with a pump fluence of 86 nJ up to (a) 10 ps and (c) 100 ps. Transient absorption spectrum of isolated aggregates up to (b) 10 ps with a 50 nJ pump fluence and (d) 100 ps with a 52 nJ pump fluence.

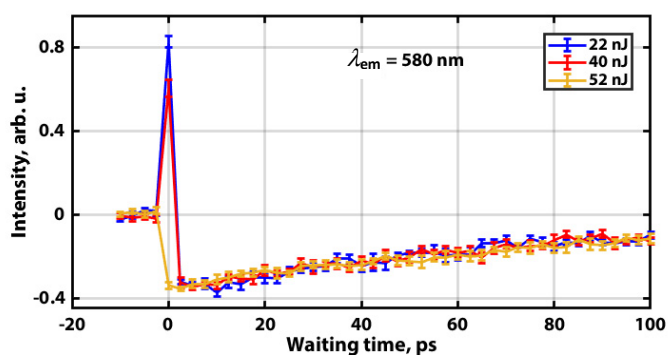


Figure S27. Time traces (normalized to last time point) with standard error plotted for the probe wavelength of 580 nm for isolated aggregates. No fluence dependence is observed during the lifetime of isolated aggregates. Averaged over $n=9$ for 22 nJ and $n=10$ for 40 nJ and 52 nJ respectively. Error bars are 1 standard error in the mean.

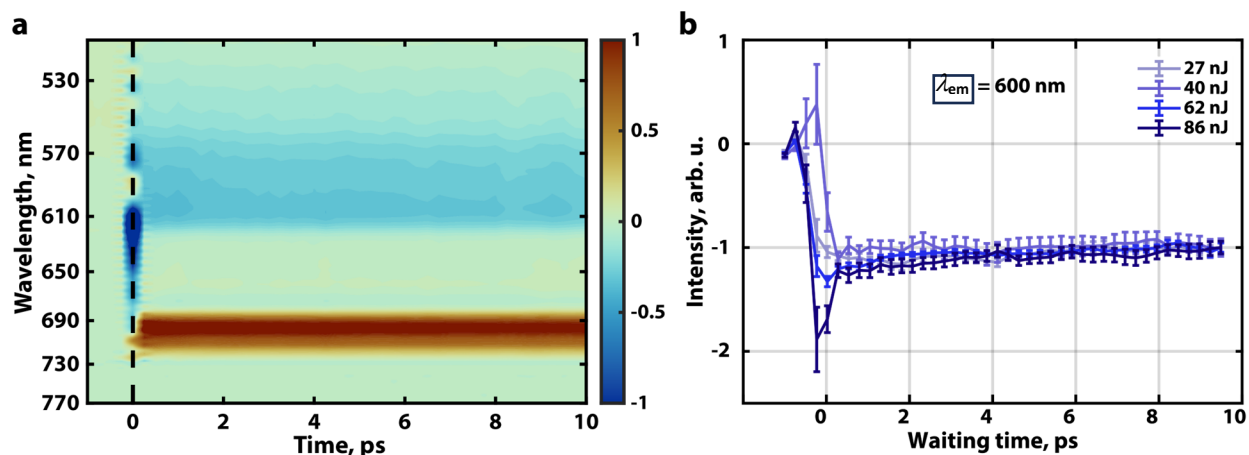


Figure S28. (a) Transient absorption spectrum of ZnOPPC monomers in anhydrous DMSO with a pump fluence of 62 nJ up to 10 ps. (b) Time traces (normalized to last time point) with standard error plotted for the probe wavelength of 600 nm for ZnOPPC monomers. No fluence dependence is observed. Averaged over $n=8$ datasets for all four fluences. Error bars are 1 standard error in the mean.

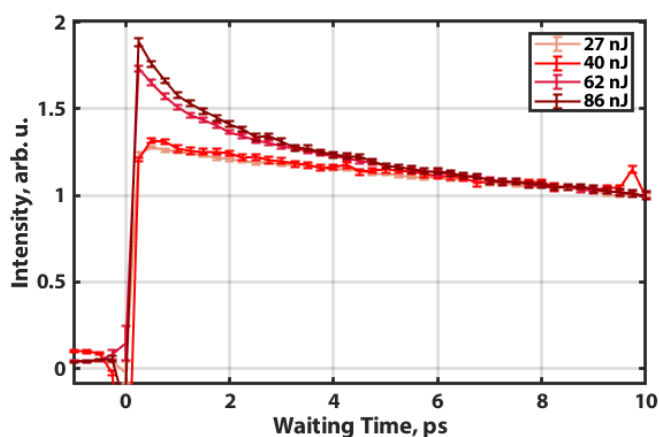


Figure S29. Time traces (normalized to last time point) with standard error plotted for the probe wavelength of 640 nm for HOFs. The positive feature also shows fluence dependence. Data for all fluences were averaged over $n=10$ datasets. Error bars are 1 standard error in the mean.

4.1. Singular value decomposition of transient absorption data of aggregates up to 10 ps

Singular value decomposition was done on transient absorption data of isolated and framework of aggregates to deconvolve the important kinetic components of the spectra. The first component largely captures the complete spectroscopic information of the dataset recorded up to 10 ps, as seen in Figures S31 and S32.

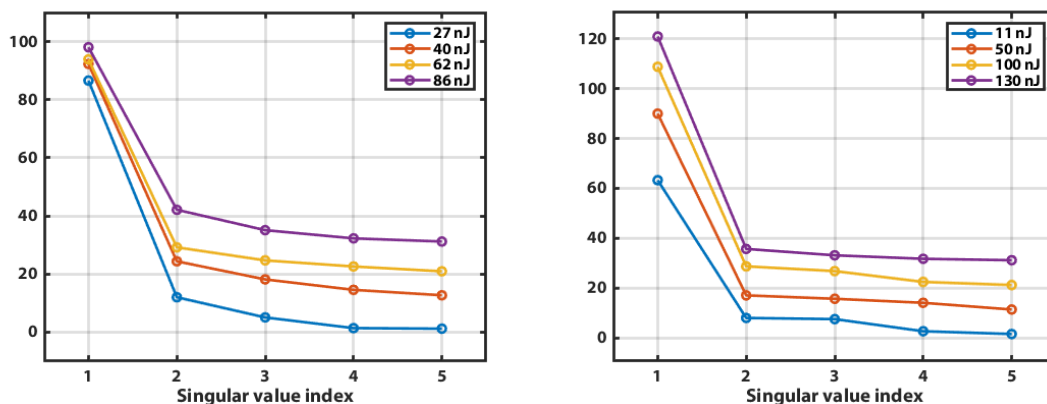


Figure S30. The first five singular values are plotted for the framework of aggregates to the left and for isolated aggregates to the right. The different fluences are separated vertically by 10 units for clarity. For example, to read the singular values of the isolated aggregates at 100 nJ, subtract 20 units from the values plotted.

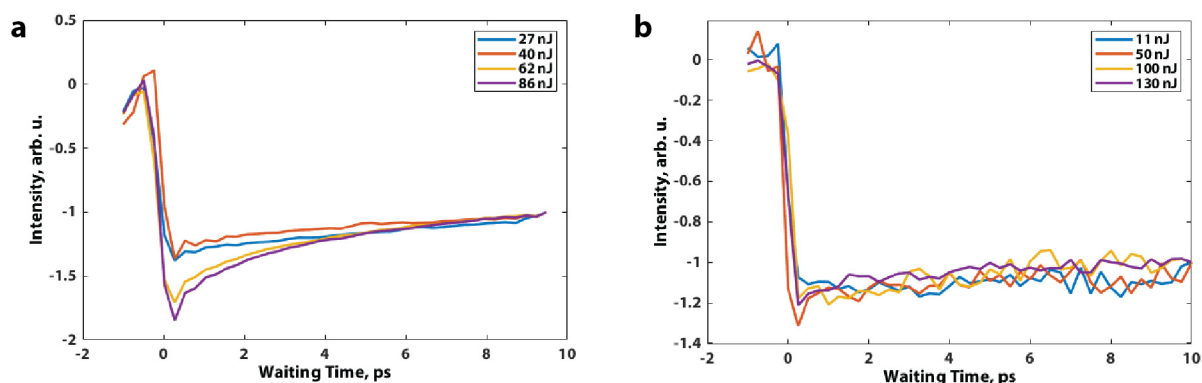


Figure S31. The first kinetic component of the framework of aggregates (a) and for isolated aggregates (b) for different pump fluences. Data is normalized to the last time point. This completely captures the behavior shown in Figure 4 in the main text.

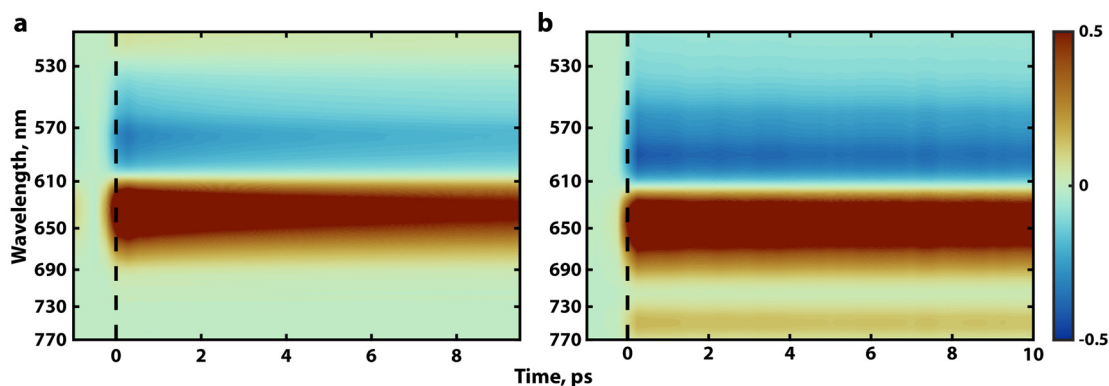


Figure S32. First SVD component for the framework of aggregates with 86 nJ pump fluence (a) and that for isolated aggregates with 130 nJ pump fluence (b). This shows that the first component largely captures the dynamics in the first 10 ps. See Figure S26 for the experimental dataset.

4.2. Calculation for coherence size in HOFs and number of excitations per HOF absorbing unit

The number of monomers in an aggregate across which an exciton is delocalized is called the coherence size. If an exciton is delocalized across N monomers, each with a transition dipole strength of μ_{mono} , the transition dipole of the aggregate exciton scales as $\sqrt{N}\mu_{\text{mono}}$. Coherence sizes have been computed previously by Scherer and co-workers for the LH2 photosynthetic protein using the following equation⁴.

$$\frac{S_{\text{B850}}}{S_{\text{B800}}} = \frac{18/N}{9} * \frac{(\sqrt{N}\mu_{\text{BChl}})^4}{\mu_{\text{BChl}}^4} \quad \text{Equation S4.1}$$

In Equation S4.1, S_{B850} and S_{B800} are the laser power normalized integrated transient absorption signals for the B800 and B850 rings of the LH2 protein. It is assumed that the excitons are not delocalized in the B800 ring and those in the B850 ring are. The B850 ring contains 18 bacteriochlorophyll (BChl) monomers while the B800 ring has 9 BChl monomers; this explains the normalization factor on the right-hand side of Equation S4.1. The right-hand side is simplified to just $2N$ i.e., the normalization factor times N .

In our case, the fluence dependent (HOFs) and independent (monomer) dynamics are in different datasets, unlike the case in LH2 as described above. Therefore, we need to calculate the number of monomers in the phase-matched excitation volume (overlap volume between the pump and probe beams inside the sample cell) for the HOF and ZnOPPC monomers transient absorption experiments – this will contribute to our normalization factor. Therefore, the coherence size, N , of the HOF is given by:

$$N = \frac{S_{\text{HOF}}}{S_{\text{mono}}} * \frac{n_{\text{mono}}}{n_{\text{HOF}}} \quad \text{Equation S4.2}$$

In Equation S4.2, n_{mono} and n_{HOF} are the number of monomers in the phase-matched volume of the monomeric and HOF solutions respectively. Equation S4.2 can be rewritten as:

$$N = \frac{S_{\text{HOF}}}{S_{\text{mono}}} \frac{c_{\text{mono}} * V}{c_{\text{HOF}} * V} * \frac{N_A / M}{N_A / M} \quad \text{Equation S4.3}$$

In Equation S4.3, c_{mono} and c_{HOF} are the concentration of the samples in g/mL; V is the phase-matched volume; N_A is Avogadro's number, and M is the molecular weight of the monomer. This equation is simplified to the following:

$$N = \frac{S_{\text{HOF}}}{S_{\text{mono}}} * \frac{c_{\text{mono}}}{c_{\text{HOF}}} \quad \text{Equation S4.4}$$

The concentration of the samples for which transient absorption data are reported in Figures S26 and S28 are 3.06×10^{-5} g/mL (c_{HOF}) and 6.21×10^{-5} g/mL (c_{mono}). The laser power normalized integrated transient absorption signal is obtained by fitting a sum of Gaussians to the transient absorption data and integrating the area under the Gaussian that fits the positive transmittance feature. The quality of fits for the spectra at a waiting time of 250 fs for a fluence of 62 nJ is shown in Figure S33. The coherence size is evaluated for the three highest pump fluences i.e., 40, 62 and 86 nJ. The coherence size obtained is $N = 11 \pm 3$.

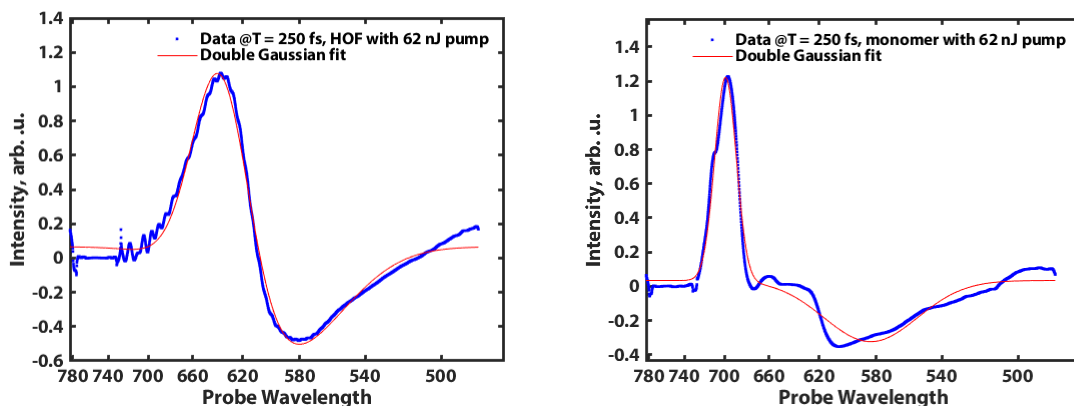


Figure S33. Fit quality shown for HOF (left) and monomer (right) spectra at $T = 250$ fs for a 62 nJ fluence.

To calculate the number of excitations per unit HOF, we perform the computation adapted from Dostal and co-workers⁵. The following equation is used to compute excitations per HOF absorbing unit:

$$n_{0,f} = \frac{f}{A_{\text{overlap}}} * \frac{\int P(\lambda) * \lambda * (1 - 10^{-A(\lambda)}) d\lambda}{hc \int P(\lambda) d\lambda} * \frac{1}{C N_A d} \quad \text{Equation S4.5}$$

Here, f is the average pump energy; A_{overlap} is the overlap area between the pump and probe pulses (see Figure S37). $P(\lambda)$ is the pump laser spectrum (see Figure 1); $A(\lambda)$ is the linear absorption spectrum of the HOF (see Figure 1); h is the Planck's constant; c is the speed of light; C is the molar concentration of the aggregate; d is the sample cell path length of 200 μm . The molar extinction coefficient of the monomer¹ is scaled by the square root of the coherence size ($N = 11$) to obtain the molar extinction coefficient of the HOF. This is used in Beer's law to obtain C . The number of excitations per rod obtained from Equation S4.5 is reported in the following table.

f (nJ)	$n_{0,f}$
27	0.47
40	0.70
62	1.09
86	1.51

Table S4.1

4.3. Fitting of time traces from transient absorption data of aggregates

4.3.1 Isolated aggregates

Transient absorption spectroscopy on the isolated aggregates did not show any fluence-dependent kinetics. Therefore, we sought to fit monoexponential kinetics of the form:

$$s(t) = A e^{-\frac{t}{\tau}} + c \quad \text{Equation S4.6}$$

to datasets up to 100 ps, where $s(t)$ is the signal at waiting time t and τ is the exponential time constant. Within 95% confidence intervals, PIA time constants for three fluences are the same (Figure S34).

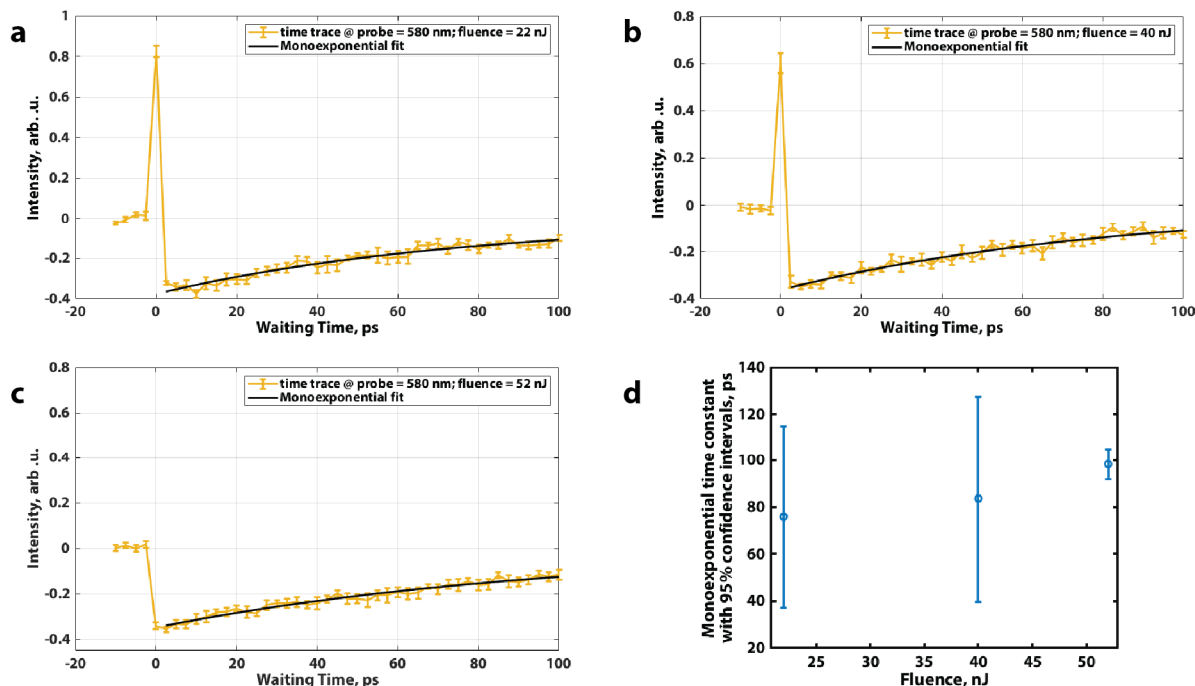


Figure S34. **a**, **b**, and **c** show transient absorption time traces of isolated aggregates up to 100 ps for a probe wavelength of 580 nm and fits with Equation S4.6. **(d)** Time constants from the fits plotted with 95% confidence intervals. Time traces are averaged over $n=9$ for 22 nJ and $n=10$ for 40 nJ and 52 nJ respectively. Error bars are 1 standard error in the mean.

4.3.2 Hydrogen-bonded framework of aggregates

We conduct second order kinetic fits to the transient absorption time traces up to 10 ps of the framework of aggregates at probe wavelength of 580 nm. The average lifetime from the three time-constants plotted in Figure S34d is 85.3 ps. Since this lifetime of the aggregate exciton is much longer than 10 ps, that lifetime will not manifest itself in the 10 ps transient absorption datasets for the framework of aggregates. Therefore, a single second order rate equation is justified for fitting for data below 10 ps.

$$s_f(t) = A \left(\frac{n_{0,f}}{1+n_{0,f}t/\tau} \right) + c \quad \text{Equation S4.7}$$

The suffix f in Equation S4.7 denotes a certain pump fluence. n_0 is the initial number of excitations per unit absorbing unit, which in this case is ~ 11 monomeric units. These equations have been used to model 5th order nonlinear signal before.^{6,7} Calculation for the $n_{0,f}$ values is reported in section 4.2 of the Supplementary information.

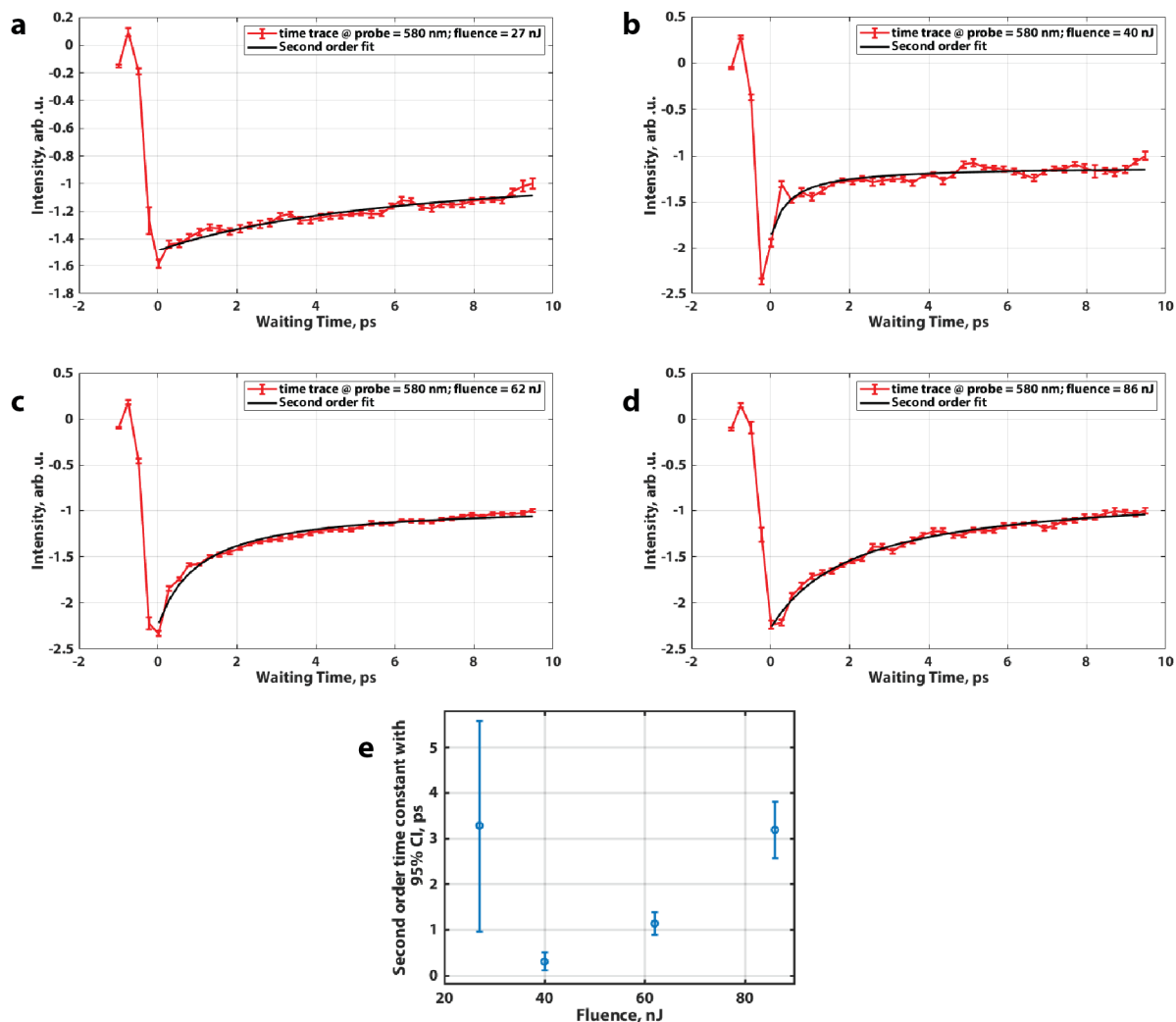


Figure S35. **a**, **b**, **c**, and **d** show transient absorption time traces of isolated aggregates up to 10 ps for a probe wavelength of 580 nm and fits with Equation S4.7. Time traces were averaged over $n=10$ datasets. Error bars are 1 standard error in the mean. **e** shows time constants from the fits plotted with 95% confidence intervals as error bars.

It is evident from the poor quality of a second order fit to the lowest (27 nJ) fluence that the 5th order signal contribution in that dataset is minimal (see Figure S35e). Overall, the 5th order signal decays at a time scale of 2-3 ps.

To further check the amount of 5th order signal in the framework of aggregates, one can subtract the 3rd order signal component from the fluence dependent time traces and plot the 5th order (in general, higher than 3rd order) residuals and confirm the presence of multiexciton dynamics in the sub-10 ps timescale. To do this, we fit Equation S4.6 to the time traces by fixing the time constant to 85.3 ps (mean value of time constants shown in Figure S34d) and only varying the parameters A and c .

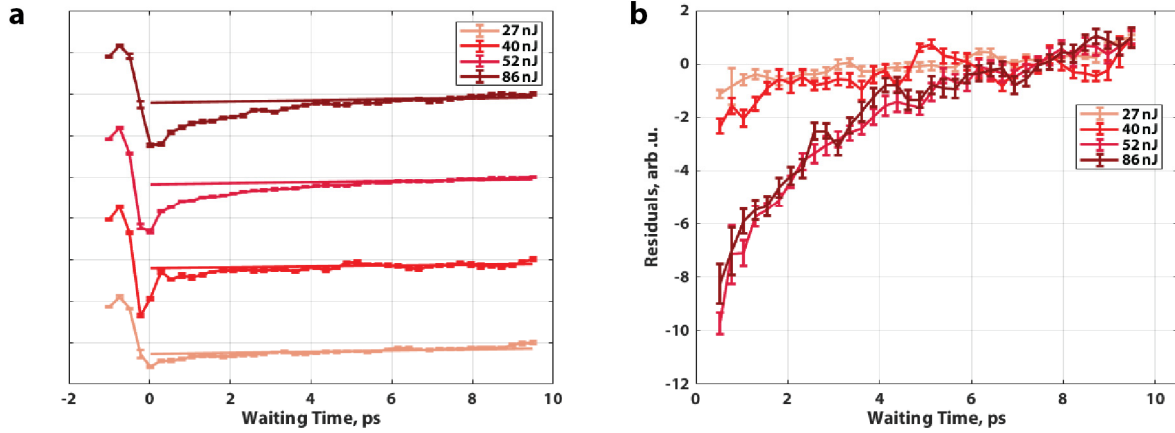


Figure S36. (a) Framework of aggregate time traces for probe wavelength of 580 nm at different fluences with Equation S4.6. Fit starting point is 1 ps for 27 nJ and 5 ps for higher fluences. (b) Residuals after the fits were subtracted from the time traces in a. Data is normalized to the last time point. Time traces were averaged over $n=10$ datasets. Error bars are 1 standard error in the mean.

The fit starting point is chosen to be 1 ps since that signal is assumed to be predominantly 3rd order, as also seen from the poor fit quality in Figure S35 for 27 nJ. The same fitting is done to the three higher fluence time traces, but the fit starting point is 5 ps, so that the fit is insensitive to the early time 5th order kinetics. The fits are plotted in Figure S36a and the residuals (after subtracting the fit from the data) are shown in Figure S36b. This shows that 5th order signal contribution increases with pump fluence. This can also be compared with the trend obtained from SVD analysis as shown in Figure S31.

We also recorded two fluence-dependent transient absorption data where sub-10 ps data were finely sampled (250 fs steps) and then sparsely (5 ps steps) till 120 ps. This data was acquired to capture the second order kinetics (annihilation) and the first order kinetics (exciton lifetime) in one dataset. Using Eq 4.5 and the procedure detailed in Section 4.2, we calculated the number of excitations per rod ($n_{0,f}$) for pump fluences 60 nJ and 98 nJ to be 1.05 and 1.72 respectively. Following the approach of Huang and coworkers, we assume a time independent rate constant of annihilation and an infinite number of absorbers such that the following solution to the differential rate equation⁸ can be used to describe the complete kinetics of the HOF aggregates.

$$n_f(t) = \frac{n_{0,f}e^{-t/\tau_1}}{1 + \tau_1\gamma_2 n_{0,f}[1 - e^{-t/\tau_1}]} \quad \text{Equation S4.8}$$

In this equation, $n_f(t)$, τ_1 and γ_2 are respectively the exciton density at time t , the first order time constant, and the second order rate constant. Equation S4.8 can be rewritten in a more linear fashion.

$$\frac{1}{n_f(t)} = \left(\frac{1}{n_{0,f}} + \tau_1\gamma_2 \right) e^{t/\tau_1} - \tau_1\gamma_2 \quad \text{Equation S4.9}$$

This equation is linear in e^{t/τ_1} . Fixing τ_1 to 85.3 ps (the exciton lifetime – see Figure S34), we fit Equation S4.9 to the inverse of the signal time traces at a probe wavelength of 580 nm for two fluences; 60 and 98 nJ. We obtain second order rate constants of 1/(2.6 ps) and 1/(2.4 ps) for the pump fluences 60 and 98 nJ

respectively. The results are shown in Figure S37. These results are in reasonable agreement with the analysis shown in Figure S35. However, it is important to note that this continuous differential equation is not rigorously appropriate for finite sized molecular systems because second order dynamics cease to be operative when only a single excitation exists on each aggregate. This issue has been studied extensively in the context of photosynthetic antenna complexes but applies generally.⁹ Unfortunately, the finite sized system formulation cannot be analytically solved, but has been shown to match the differential rate laws in all important limits such as short time (second order kinetics), long time (first order kinetics), as well as the limit above of an infinitely connected system with continuous excitation density. For these reasons, we favor extracting the chemically intuitive rate and time constants from early dynamics when second order processes dominate and later times when first order processes dominate.

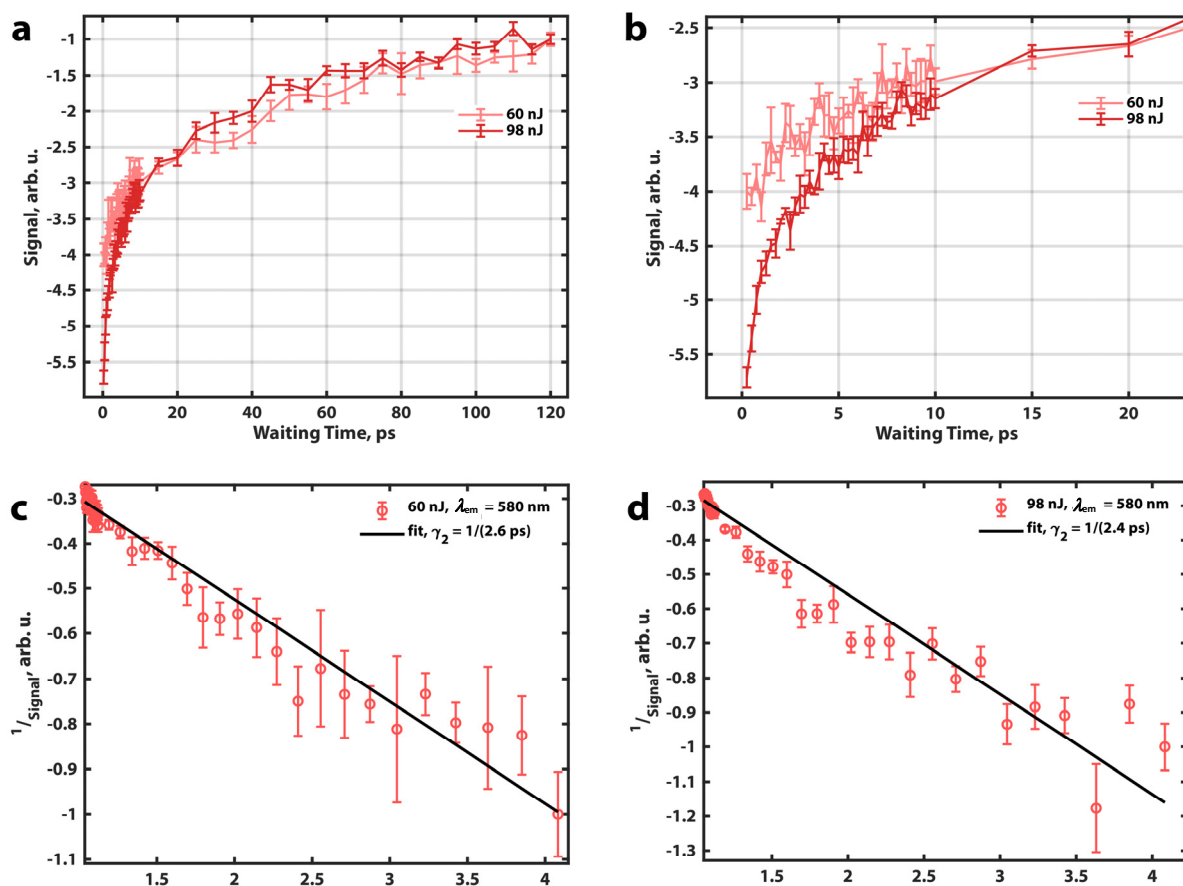


Figure S37. (a) Time traces at $\lambda_{\text{em}} = 580 \text{ nm}$ for fluences 60 nJ and 98 nJ normalized to the last time point. (b) Panel a zoomed in the first 20 ps. (c) Quality of fit of Equation S4.9 to data at 60 nJ yielding a second order rate constant of $1/(2.6 \text{ ps})$. (d) Quality of fit of Equation S4.9 to data at 98 nJ yielding a second order rate constant of $1/(2.4 \text{ ps})$. Time traces were averaged over $n=5$ datasets. Error bars are 1 standard error in the mean.

Suppl. Note 5. Beam size and fifth order signal contributions

The beam size was calculated from the diameter of $211\mu\text{m}$ (Figure S37) to be 0.14 mm^2 , assuming a circular pulse front with a Gaussian intensity variation.

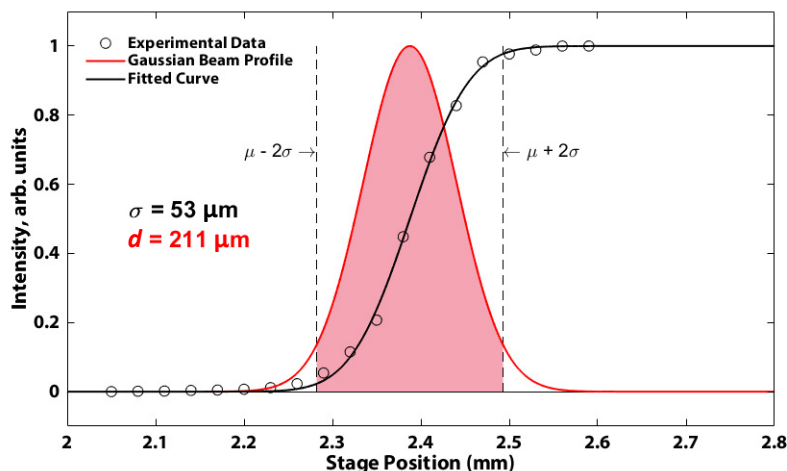


Figure S38. Beam diameter measured at the sample position by recording the power transmitted as a function of the micrometer that moves the sample stage and thereby a razor blade that partially blocks the beam as the micrometer is changed. The data was fit to an error function whose derivative estimated a Gaussian curve. The diameter of the beam, estimated as four times the standard deviation of the Gaussian, is estimated to be $211\mu\text{m}$ for all fluence dependent transient absorption spectra.

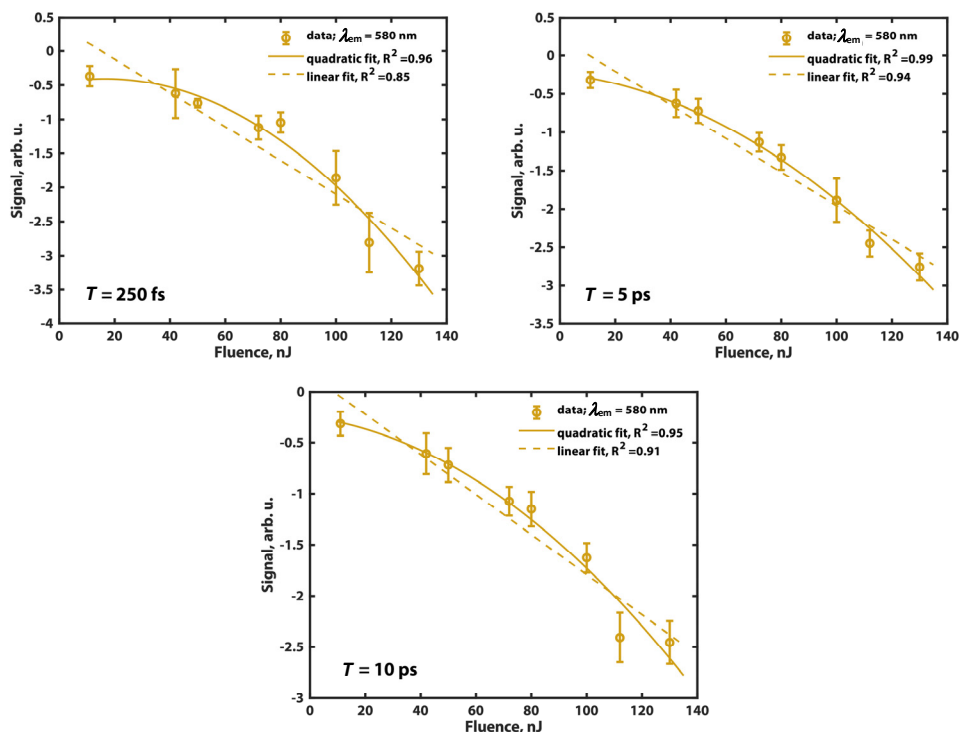


Figure S39. Figure showing the probe intensity normalized signal intensity recorded at a waiting time of 250 fs, 5 ps and 10 ps, with pump fluence at a detection wavelength of 580 nm for the isolated aggregates. The nonlinear signal dependence with power confirms that multiple excitations are created and sustained in the picosecond timescale. Number of runs averaged over for different fluences: $n=40$ (11 nJ), $n=20$ (42 nJ), $n=10$ (72 nJ, 80 nJ), $n=7$ (100 nJ, 112 nJ), $n=6$ (130 nJ). Error bars are 1 standard error in the mean.

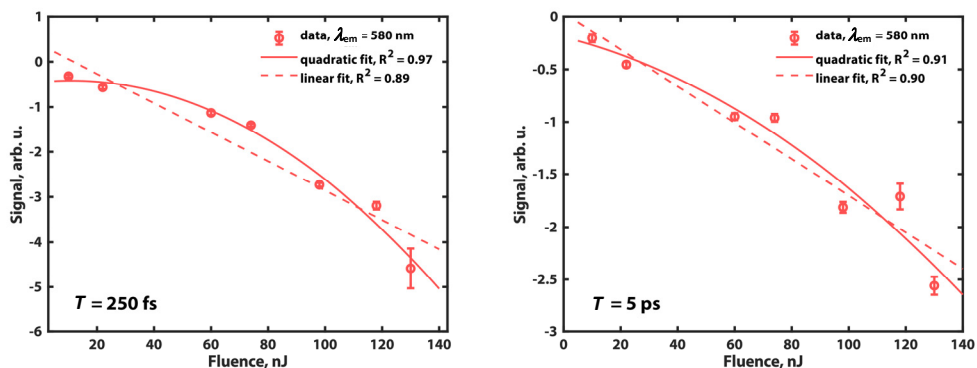


Figure S40. Figure showing the probe intensity normalized signal intensity recorded at a waiting time of 250 fs and 5 ps with pump fluence at a detection wavelength of 580 nm for the HOF. The quadratic component of the signal with fluence is significantly diminished by a waiting time of 5 ps due to annihilation of the biexcitons in a timescale of 2-3 ps. Number of runs averaged over for different fluences: $n=7$ (10 nJ, 22 nJ), $n=5$ (60 nJ), $n=7$ (74 nJ), $n=5$ (98 nJ), $n=7$ (118 nJ), $n=4$ (130 nJ). Error bars are 1 standard error in the mean.

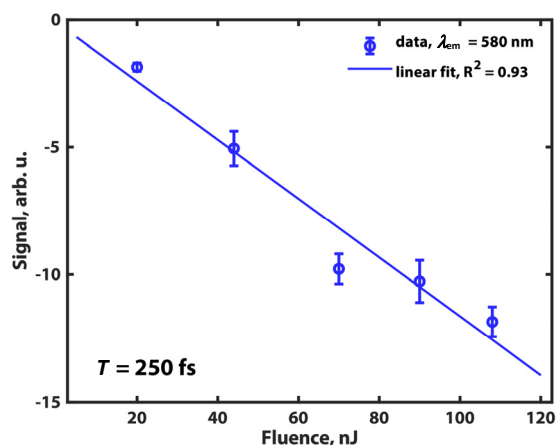


Figure S41. Figure showing the probe intensity normalized signal intensity recorded at a waiting time of 250 fs with pump fluence at a detection wavelength of 580 nm for the monomer. The linearity of the signal indicates an absence of multiparticle dynamics. $n=10$ (20 nJ), $n=5$ (44 nJ, 70 nJ, 90 nJ, 108 nJ). Error bars are 1 standard error in the mean.

Suppl. Note 6. Electronic structure calculation to estimate the HOF lattice arrangement

A Density Functional Theory (DFT) calculation was carried out using Gaussian 16, Revision A. 03.¹⁰ The structure of a ZnOPPc monomer was optimized by using the B3LYP functional and the D3(BJ) dispersion correction in gas phase. The 6-31G* basis set was used for C, H, O and N atoms and SDD was used for the Zn atoms. Frequency analysis was conducted at the same level of theory to verify that we obtained an energetic minimum.

ZnOPPc monomer optimized geometry:

C	-3.41230	-10.07510	0.22910
C	-1.78580	-7.78960	0.07530
C	-0.95170	-6.56260	0.00030
C	-0.85540	-4.15540	-0.01850
C	0.55350	-4.20560	-0.01100
C	0.47590	-6.61330	-0.01790
C	1.22010	-7.89710	-0.08650
C	2.69670	-10.29290	-0.23820
C	3.42290	-11.59620	-0.35860
O	2.94810	-12.57390	-0.88600
O	4.67960	-11.64600	0.16210
H	4.97600	-10.75310	0.40120

C	1.02320	-2.82350	-0.01290
N	-0.07250	-1.99370	-0.01710
C	-1.22490	-2.74300	-0.01970
N	2.30580	-2.47510	-0.00910
C	2.74480	-1.22080	-0.00710
N	1.99560	-0.06830	-0.00650
C	2.82530	1.02750	-0.00230
C	4.20770	0.55770	0.00100
C	4.15700	-0.85120	-0.00530
N	2.47690	2.31000	-0.00040
C	1.22260	2.74910	-0.00440
N	0.07030	1.99980	-0.00920
C	-1.02550	2.82970	-0.01330
C	-0.55580	4.21210	-0.01090
C	0.85310	4.16160	-0.00690
N	-2.30800	2.48120	-0.01580
C	-2.74700	1.22680	-0.01800
N	-1.99780	0.07450	-0.02040
C	-2.82760	-1.02140	-0.02230
C	-4.20990	-0.55180	-0.01980
C	-4.15930	0.85720	-0.01910
N	-2.47920	-2.30380	-0.02240
C	-6.56590	0.95270	0.00210
C	-6.61730	-0.47470	-0.02780
C	0.94910	6.56850	0.00520
C	-0.47820	6.61960	-0.02870
C	6.56380	-0.94730	0.01040
C	6.61520	0.48000	-0.00900
C	-7.90240	-1.21620	-0.10300
C	-7.79320	1.78470	0.09000
C	-10.30410	-2.66700	-0.25300
C	-10.09030	3.40690	0.26780
C	-11.59370	-3.39170	-0.36960
C	-11.28130	4.31220	0.31750
O	-12.47050	-3.12460	-1.16730
O	-11.71330	-4.40860	0.52130
O	-11.27470	5.44100	-0.11320
O	-12.40980	3.80420	0.88290

H	-12.58670	-4.80720	0.35030
H	-12.30990	2.84890	1.02500
C	1.78180	7.79590	0.08700
C	-1.21870	7.90440	-0.11820
C	3.40580	10.08210	0.25870
C	7.79140	-1.78040	0.08660
C	7.90070	1.22070	-0.08460
C	10.07500	-3.40940	0.24750
C	11.30210	-4.23400	0.37480
O	11.36640	-5.23420	-0.54070
H	12.20580	-5.69830	-0.36460
O	12.17460	-4.05750	1.20170
C	4.29000	11.27340	0.30150
O	5.24140	11.45850	-0.43110
O	3.93210	12.16480	1.26020
H	4.57310	12.89650	1.19170
C	-4.29730	-11.26620	0.26190
O	-3.95370	-12.15480	1.22780
O	-5.23780	-11.45300	-0.48440
H	-4.59190	-12.88810	1.15090
Zn	-0.00120	0.00320	-0.01540
C	-2.67140	10.31250	-0.30290
C	10.30900	2.67540	-0.24350
C	-3.40150	11.60990	-0.46310
C	11.60370	3.41220	-0.39190
O	-4.14500	12.02950	0.59640
H	-3.96460	11.47450	1.37200
O	12.02820	4.12580	0.68630
H	11.48350	3.91390	1.46130
O	-3.35190	12.27780	-1.46850
O	12.26400	3.39460	-1.40340
C	9.33630	3.01510	0.70500
H	9.47740	3.86260	1.37150
C	10.05550	1.61990	-1.13010
H	10.80220	1.38570	-1.88080
C	8.14460	2.29820	0.77910
H	7.39840	2.56630	1.52100
C	8.87450	0.89650	-1.04500

H	8.69470	0.07560	-1.73050
C	8.77820	-1.53490	1.05650
H	8.65220	-0.70960	1.74890
C	9.90530	-2.34050	1.13770
H	10.66950	-2.16170	1.88620
C	9.09680	-3.66610	-0.72050
H	9.22890	-4.48950	-1.41280
C	7.96500	-2.85950	-0.79420
H	7.21370	-3.05020	-1.55480
C	5.42760	1.22420	-0.00340
H	5.46040	2.30800	-0.03950
C	5.32570	-1.60360	0.00070
H	5.28130	-2.68710	0.03240
C	1.21970	-5.42550	-0.01300
H	2.30360	-5.45820	-0.04620
C	-1.60770	-5.32410	-0.01160
H	-2.69120	-5.27970	0.01960
C	-2.86870	-7.95790	-0.80320
H	-3.06280	-7.20260	-1.55890
C	-1.53760	-8.78110	1.03860
H	-0.71040	-8.65930	1.72940
C	-3.67230	-9.08970	-0.73040
H	-4.50340	-9.23330	-1.41230
C	-2.34060	-9.91240	1.11740
H	-2.14310	-10.67180	1.86480
C	0.89520	-8.88310	-1.03420
H	0.06970	-8.71530	-1.71710
C	2.29280	-8.13390	0.78550
H	2.53660	-7.39490	1.54270
C	3.02240	-9.31780	0.71280
H	3.81450	-9.48740	1.43840
C	1.61710	-10.06620	-1.10300
H	1.36420	-10.83400	-1.82590
C	-8.14670	-2.28970	0.76790
H	-7.40310	-2.54570	1.51680
C	-9.33610	-3.00910	0.69880
H	-9.52050	-3.83010	1.38200
C	-8.87770	-0.88790	-1.06030

H	-8.69720	-0.06830	-1.74730
C	-10.06370	-1.60460	-1.13510
H	-10.81970	-1.36110	-1.87360
C	-5.42950	-1.21850	-0.02690
H	-5.46300	-2.30210	-0.06640
C	-5.32790	1.60950	-0.00570
H	-5.28260	2.69270	0.03510
C	-7.95880	2.89310	-0.75670
H	-7.19990	3.10960	-1.50260
C	-8.78710	1.51560	1.04390
H	-8.66380	0.68070	1.72470
C	-9.92130	2.31440	1.13040
H	-10.65110	2.10110	1.90780
C	-9.08800	3.69850	-0.66480
H	-9.21880	4.55710	-1.31420
C	-1.22230	5.43180	-0.02520
H	-2.30570	5.46420	-0.07130
C	1.60540	5.33020	0.00340
H	2.68860	5.28590	0.04420
C	1.52160	8.78830	1.04620
H	0.68590	8.66610	1.72680
C	2.32340	9.91960	1.13410
H	2.11790	10.67930	1.87930
C	3.67770	9.09590	-0.69670
H	4.51690	9.23910	-1.36860
C	2.87540	7.96370	-0.77820
H	3.07890	7.20790	-1.53090
C	-0.88060	8.87640	-1.07560
H	-0.04970	8.69590	-1.74870
C	-1.60220	10.05750	-1.17280
H	-1.35610	10.80350	-1.92030
C	-3.02600	9.34050	0.64070
H	-3.88420	9.48080	1.29380
C	-2.30970	8.14930	0.72810
H	-2.58910	7.40460	1.46720

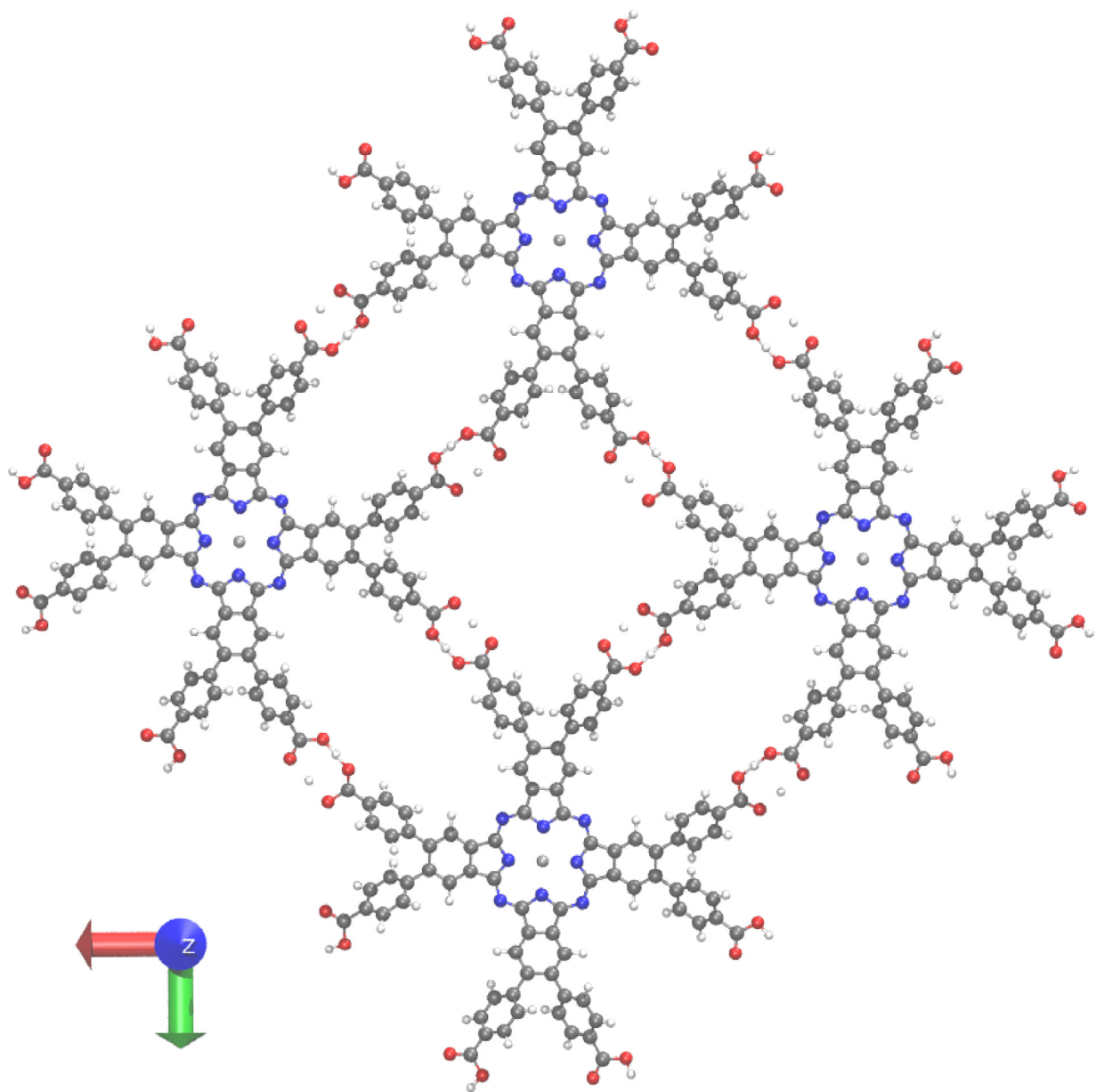


Figure S42: Orthographic top view of π -stacked units of four H-bonded ZnOPPC monomers.

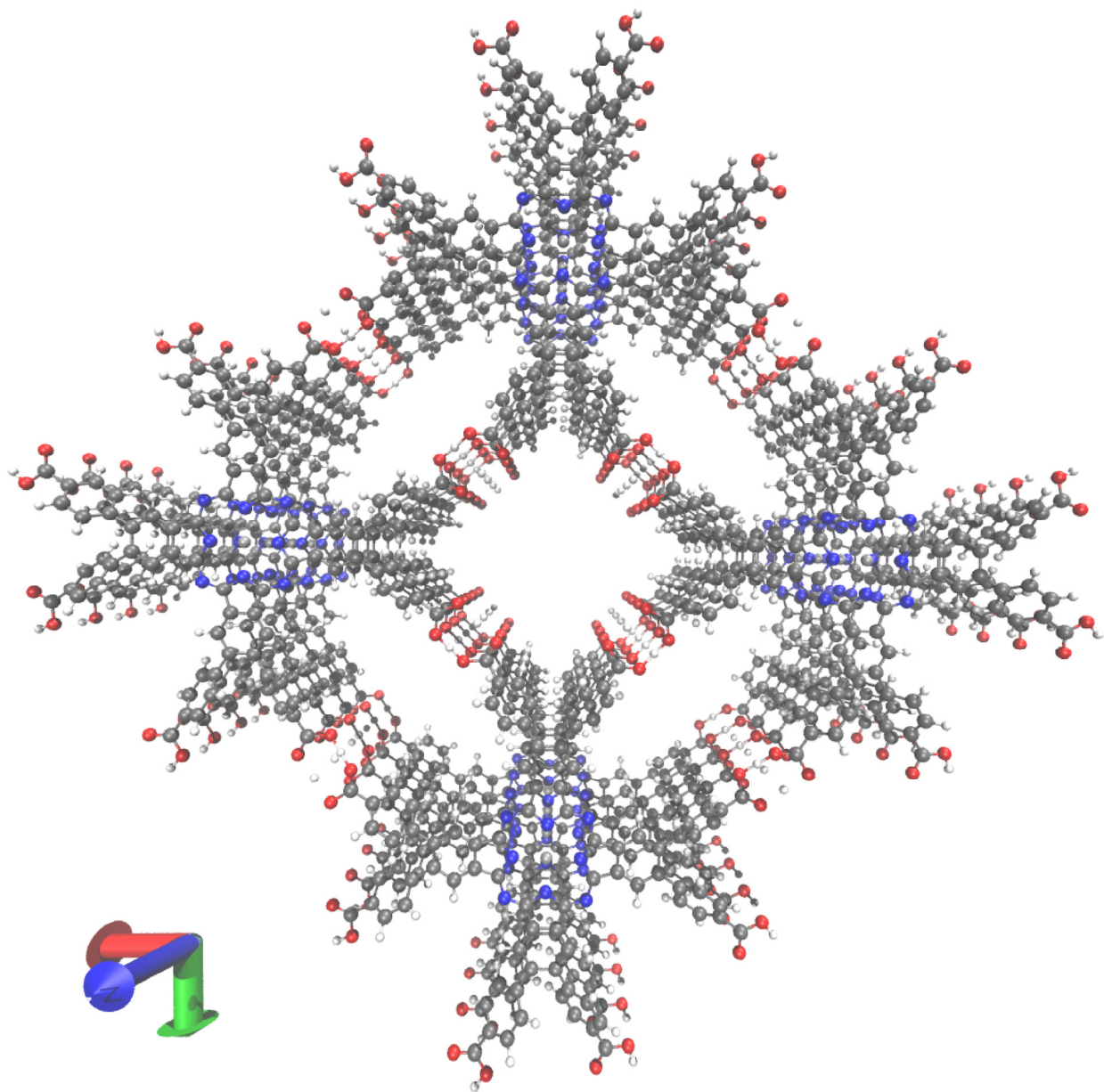


Figure S43: Perspective top view of π -stacked units of four H-bonded ZnOPPC monomers.

After the structure of the ZnOPPC monomer was optimized, a hydrogen bonding framework structure was proposed, which allowed the maximum number of hydrogen bonding between adjacent ZnOPPC monomers. In this model, the a value (lattice parameter) of the lattice was measured to be 25.6 Å, which was consistent as the estimated a value from the PXRD pattern. Different layers were arranged in a π -stacked fashion, and the c value of the lattice was set to be 4 Å.

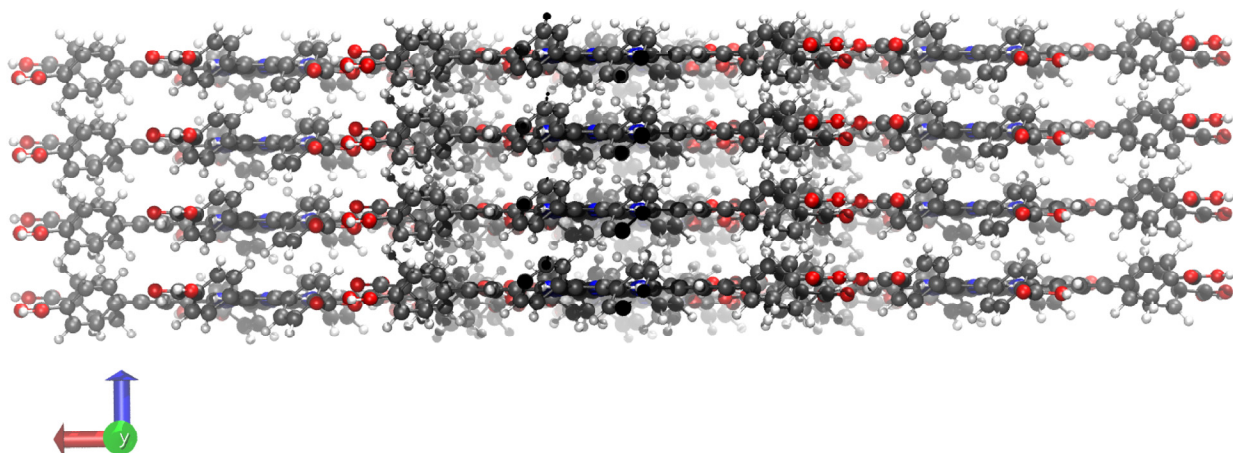


Figure S44: Orthographic side view of π -stacked units of four H-bonded ZnOPPC monomers.

Supplementary references

- (1) Luo, T.; Nash, G. T.; Xu, Z.; Jiang, X.; Liu, J.; Lin, W. Nanoscale Metal–Organic Framework Confines Zinc-Phthalocyanine Photosensitizers for Enhanced Photodynamic Therapy. *J. Am. Chem. Soc.* **2021**, *143* (34), 13519–13524. <https://doi.org/10.1021/jacs.1c07379>.
- (2) Zheng, H.; Caram, J. R.; Dahlberg, P. D.; Rolczynski, B. S.; Viswanathan, S.; Dolzhenkov, D. S.; Khadivi, A.; Talapin, D. V.; Engel, G. S. Dispersion-Free Continuum Two-Dimensional Electronic Spectrometer. *Appl. Opt.* **2014**, *53* (9), 1909. <https://doi.org/10.1364/AO.53.001909>.
- (3) Šanda, F.; Perlík, V.; Lincoln, C. N.; Hauer, J. Center Line Slope Analysis in Two-Dimensional Electronic Spectroscopy. *J. Phys. Chem. A* **2015**, *119* (44), 10893–10909. <https://doi.org/10.1021/acs.jpca.5b08909>.
- (4) Book, L. D.; Ostafin, A. E.; Ponomarenko, N.; Norris, J. R.; Scherer, N. F. Exciton Delocalization and Initial Dephasing Dynamics of Purple Bacterial LH2. *J. Phys. Chem. B* **2000**, *104* (34), 8295–8307. <https://doi.org/10.1021/jp000485d>.
- (5) Dostál, J.; Fennel, F.; Koch, F.; Herbst, S.; Würthner, F.; Brixner, T. Direct Observation of Exciton–Exciton Interactions. *Nat. Commun.* **2018**, *9* (1), 2466. <https://doi.org/10.1038/s41467-018-04884-4>.
- (6) Sun, D.; Rao, Y.; Reider, G. A.; Chen, G.; You, Y.; Brézin, L.; Harutyunyan, A. R.; Heinz, T. F. Observation of Rapid Exciton–Exciton Annihilation in Monolayer Molybdenum Disulfide. *Nano Lett.* **2014**, *14* (10), 5625–5629. <https://doi.org/10.1021/nl5021975>.

- (7) Navotnaya, P.; Sohoni, S.; Lloyd, L. T.; Abdulhadi, S. M.; Ting, P.-C.; Higgins, J. S.; Engel, G. S. Annihilation of Excess Excitations along Phycocyanin Rods Precedes Downhill Flow to Allophycocyanin Cores in the Phycobilisome of *Synechococcus Elongatus* PCC 7942. *J. Phys. Chem. B* **2022**, *126* (1), 23–29. <https://doi.org/10.1021/acs.jpcc.1c06509>.
- (8) Yuan, L.; Huang, L. Exciton Dynamics and Annihilation in WS₂ 2D Semiconductors. *Nanoscale* **2015**, *7* (16), 7402–7408. <https://doi.org/10.1039/C5NR00383K>.
- (9) Gülen, D. Theory of Exciton Annihilation in Complexes of a Finite Number of Molecular Sites. *Math. Biosci.* **1990**, *102* (1), 21–39. [https://doi.org/10.1016/0025-5564\(90\)90054-3](https://doi.org/10.1016/0025-5564(90)90054-3).
- (10) Gaussian 16, Revision A.03, Frisch, M. J.; Trucks, G. W.; Schlegel, H. B.; Scuseria, G. E.; Robb, M. A.; Cheeseman, J. R.; Scalmani, G.; Barone, V.; Petersson, G. A.; Nakatsuji, H.; Li, X.; Caricato, M.; Marenich, A. V.; Bloino, J.; Janesko, B. G.; Gomperts, R.; Mennucci, B.; Hratchian, H. P.; Ortiz, J. V.; Izmaylov, A. F.; Sonnenberg, J. L.; Williams-Young, D.; Ding, F.; Lipparini, F.; Egidi, F.; Goings, J.; Peng, B.; Petrone, A.; Henderson, T.; Ranasinghe, D.; Zakrzewski, V. G.; Gao, J.; Rega, N.; Zheng, G.; Liang, W.; Hada, M.; Ehara, M.; Toyota, K.; Fukuda, R.; Hasegawa, J.; Ishida, M.; Nakajima, T.; Honda, Y.; Kitao, O.; Nakai, H.; Vreven, T.; Throssell, K.; Montgomery, J. A., Jr.; Peralta, J. E.; Ogliaro, F.; Bearpark, M. J.; Heyd, J. J.; Brothers, E. N.; Kudin, K. N.; Staroverov, V. N.; Keith, T. A.; Kobayashi, R.; Normand, J.; Raghavachari, K.; Rendell, A. P.; Burant, J. C.; Iyengar, S. S.; Tomasi, J.; Cossi, M.; Millam, J. M.; Klene, M.; Adamo, C.; Cammi, R.; Ochterski, J. W.; Martin, R. L.; Morokuma, K.; Farkas, O.; Foresman, J. B.; Fox, D. J. *Gaussian, Inc.*, Wallingford CT, **2016**.